Proton Chemical Exchange Saturation Transfer (CEST) MRS and MRI

Peter C.M. van Zijl[1,2] & Akansha Ashvani Sehgal[1,2]

[1] *The Johns Hopkins University School of Medicine, Baltimore, MD, USA*
[2] *Kennedy Krieger Institute, Baltimore, MD, USA*

Proton magnetic resonance spectroscopy (^{1}H MRS) of biological systems has higher specificity than MRI because resonances of multiple metabolites can be distinguished, reflecting chemistry and physiology in situ. Unfortunately, this approach has very low sensitivity as the metabolites are typically at millimolar concentrations compared to the molar signal strength of water-based MRI. As a consequence, even though ^{1}H MRS is a powerful and common research tool, its inroad into daily clinical practice has been limited. Until very recently, ^{1}H MRS applications have focused on the resonances upfield (i.e., at lower frequency) of the water resonance. This article deals with protons that are generally not observed in a typical water-suppressed spectrum, namely, the exchangeable protons found predominantly downfield from water. These can usually be detected by MRS only if the transfer of water proton saturation (established during water suppression) is not a confounding factor, or by using water exchange (WEX) spectroscopy, in which RF labeling of the water protons is transferred to the exchangeable protons and subsequently detected. More importantly, it has recently become clear that the presence of such exchangeable protons on low concentration solute molecules can be detected via the water signal by RF labeling of these protons and subsequent transfer of this label to water protons. This process, leading to saturation of the water signal and enhancement of the effect through repeated exchange, can be used for the imaging of metabolite signals or exchangeable-proton-based contrast agents with enhanced sensitivity. This has given rise to the field of chemical exchange saturation transfer (CEST) MRI, which has greatly increased the potential for translating spectroscopic methods to the clinic. Examples include the measurement of pH, temperature, and enzyme activity as well as detection of cellular metabolites, ions, and proteins and peptides. In addition, bio-organic compounds can now be used for contrast agents, cell and nanoparticle labeling, and reporter genes.

Keywords: chemical exchange saturation transfer (CEST), water exchange (WEX), amide, amine, hydroxyl, imino

How to cite this article:
eMagRes, 2016, Vol 5: 1307 – 1332. DOI 10.1002/9780470034590.emrstm1482

Introduction

Proton magnetic resonance spectroscopy (^{1}H MRS) of biological systems has existed for many decades, but despite its great chemical and metabolic specificity and its proven use in research, it has made little progress into routine clinical practice. There are several causes for this, the main one being that signal sensitivity limits its use to detecting millimolar (mM) concentrations of small metabolites. An improved signal-to-noise ratio (SNR) can be achieved by increasing the size of the volume elements (voxels), but this reduces spatial specificity. While nuclei such as ^{31}P can provide spectra that illuminate physiological processes and pH in research applications, the only nucleus that has come close to routine clinical use is the proton, basically because clinical MRI is geared toward the use of the water protons for high-resolution imaging. Unfortunately, ^{1}H MRS is not simple and requires suppression of the large water signal (see ***Single-Voxel MR Spectroscopy***; ***CSI and SENSE CSI***). In addition, the coupled protons of many different metabolites resonate over a small chemical shift range, leading to overlapping signals that are difficult to separate or quantify, unless specific editing approaches are used (see ***Spectral Editing***). In addition, the spectral information is often unavailable immediately for the physician to look at, but requires further advanced data analysis. This is often too much work for clinical practice, where patients spend perhaps 15–30 min in the scanner, during which the maximum possible information needs to be gathered. As many fast anatomical and physiological imaging methods are already available, MRS is generally not performed, except at high-end research centers. This is unfortunate as the proton spectrum contains a wealth of information regarding important metabolites such as Cr, Cho, NAA, MI, Glu, Gln, GABA, gluthatione, glucose, lactate, and alanine, just to mention a few.

Currently, the bulk of ^{1}H MRS efforts are focused on the signals upfield (i.e., at lower frequency) relative to the water resonance, where the aliphatic protons resonate. The spectral region downfield from water contains aromatic and exchangeable protons (e.g., amide, imino, amine and hydroxyl protons) but typically, little signal is detected there. The reason for the low level of aromatic signals is the low concentration of such protons, but for exchangeable protons there are two more subtle causes.[1] The first and foremost is the suppression of the water ^{1}H signal during ^{1}H MRS, which imparts some level of saturation on the water signal. In the case of complete saturation

of the abundant water protons 'w', every exchange of a solute proton 's' leads to replacement by a saturated water proton from the large pool. This causes an enhancement of signal disappearance with the solute-to-water proton exchange rate k_{sw}, leading to 'apparent' fast relaxation, both transverse and longitudinal, with rates of $r_{2s} = (R_{2s}) + k_{sw}$, and $r_{1s} = (R_{1s}) + k_{sw}$, respectively, with $R_2 = 1/T_2$ and $R_1 = 1/T_1$ as the spin–spin and spin–lattice relaxation rates in the absence of exchange. A second issue for such protons is that the linewidth is approximately proportional to the exchange rate (LW $\sim k_{sw}/\pi$), which lowers their SNR. Solutions for this problem can be found by designing specific pulse sequences, which is discussed in the section titled 'MRS of Exchangeable Protons'.

Because of the above issues, the use of exchangeable protons in the ^{1}H spectrum for obtaining clinical information seems even more unlikely than that of aliphatic protons.[1–6] However, this outlook changed dramatically with the advent of chemical exchange saturation transfer (CEST) spectroscopy and imaging, first suggested by Balaban *et al.*[7–9] This approach, based on the saturation transfer principles outlined by Forsen and Hoffman,[10] allows the detection of exchangeable protons by saturating them and following the transfer of saturation to the water signal. In contrast to the direct detection of exchangeable protons in MRS, the exchange with water in this case functions as a sensitivity enhancer because the nonsaturated protons of the large solvent pool continuously replace the saturated solute protons, which are again saturated and undergo fast exchange in a process that benefits from fast exchange with water. Provided that sufficient saturation is imparted while the protons are on the solute and many exchanges take place during the saturation period, an increasing saturation of the water signal occurs with a rate proportional to the product of the solute proton concentration, the saturation efficiency, and k_{sw}. Early CEST papers[7,11–14] showed that enhancements of the order of 10–10 000 can be achieved by this process, giving rise to new possibilities for imaging low concentration metabolites and contrast materials based on the water protons. Contrary to the well-known magnetization transfer contrast (MTC) of protons in semisolid tissues, the transfer process from mobile species has greater potential because the lifetime of the protons in terms of their T_2s is much longer, allowing the use of pulsed editing approaches.

This burgeoning field is just starting and the outlook is promising.[15–24] In this article, after an overview of the principles underlying the detection of exchangeable protons in MRS (see section titled 'MRS of Exchangeable Protons') and the opposite process in CEST-MRI (see section titled 'Chemical Exchange Saturation Transfer (CEST)'), the different types of pulse sequences that are available for CEST (see section titled 'Pulsed Sequences for MTC and CESTMRI') and issues that may affect data analysis (see section titled 'Data Analysis for CEST Spectra') are described. The section titled 'Potential and Clinical Translation of CEST Methods' briefly summarizes some important applications that are already being translated to human scanners. However, because of the availability of excellent recent reviews of CEST applications, the development of CEST agents, and the study of endogenous CEST contrast,[15–24] this article will focus on the relationship between MRS of exchangeable protons and CEST MRI, and on the pulse sequences used for detecting CEST effects.

MRS of Exchangeable Protons

Detecting Exchangeable Protons with MRS

In the ^{1}H spectrum most exchangeable protons are shifted downfield of water and overlap with aromatic signals. However, as noted above, not much signal is detected there owing to water suppression and the transfer of saturated protons from water to the metabolites. In order to detect these protons, one has to avoid presaturation and instead perform water suppression rapidly at the time of detection, before saturation can be transferred. Also, the echo time (TE) in the sequence needs to be minimized to avoid signal reduction due to the short apparent T_2.

The effect of a composite so-called WATERGATE[25] refocusing pulse ($3 - 9 - 19 - \overline{19} - \overline{9} - \overline{3}$) used to suppress the water signal in an outer-volume suppressed (OVS) point-resolved spectroscopy (PRESS) spectrum in vivo is illustrated in Figure 1. While adding a third echo-refocusing period to the sequence just before detection (top) lengthens the TE, many resonances remain visible (Figure 1a). However, when a chemical shift-selective (CHESS) water suppression pulse is added before the sequence (bracketed at top), several signals are suppressed (Figure 1b). Similarly, on adding a so-called DRYSTEAM sequence[26] during the middle period, (TM = 50 ms between the second and third PRESS pulse), in addition to the CHESS water suppression, most signals downfield disappear (Figure 1c) due to saturation transfer during these periods. However, when the OVS–PRESS–WATERGATE sequence is applied postmortem (Figure 1d), many resonances, especially in the 8–8.5 ppm region, increase in intensity. This is attributed to a drop in pH and the sensitivity of backbone amide protons in proteins and peptides to pH in the physiological range.[27,28] A point of importance for metabolite quantification is that water saturation reduces the signals of not only exchangeable protons but also some of the metabolites (e.g., Cr, NAA and lactate) due to their interaction with the immobile semi-solid tissue matrix.[29–34] This complicates the use of, for instance, Cr as a concentration standard.

It is important to point out that whenever water suppression is used, one cannot shorten the repetition time (TR) between scans below the limit at which the water saturation from the previous scan reduces the exchangeable proton signal. Thus, the best approach for observing exchangeable protons would be to avoid exciting the water at all. This can be achieved either by using selective water flip-back approaches after general excitation,[35,36] or by selectively exciting only the spectral region of interest. The latter can be done using a 'metabolite cycling' approach[37,38] where the downfield and upfield resonances are inverted in an alternating manner, followed by signal subtraction. The downfield spectrum resulting from applying this approach in a human brain,[5] shown in Figure 2 (inset), is very similar to that found in the cat brain by Mori *et al.* (Figure 1a and b). Adding a CHESS water suppression pulse before this sequence elicited a signal reduction in the 8–8.5 ppm region very similar to that shown in Figure 1.

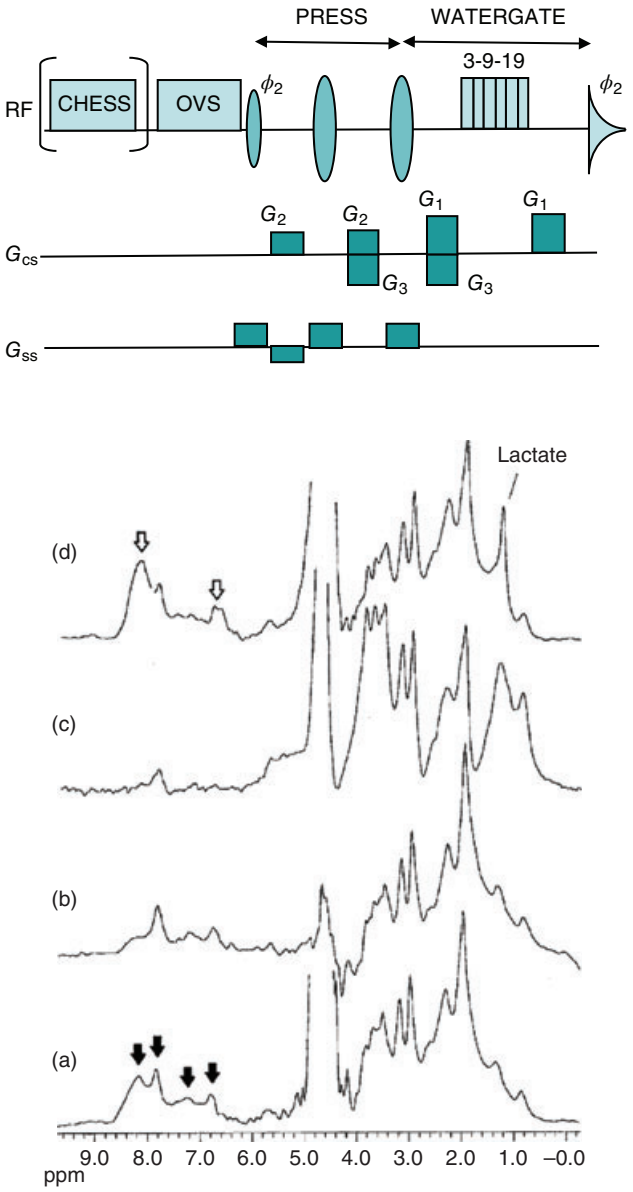

Figure 1. Top: OVS–PRESS–WATERGATE sequence used to acquire the in vivo spectra with exchangeable protons shown in parts a, b, and d. The phase ϕ_2 was cycled as (0°, 180°). G_{cs} and G_{ss} indicate slice and coherence selection, respectively. The (x, y, z) gradient strengths (in G/cm) for G_1, G_2, and G_3 gradient pulses were (10,4,1), (8,8,6), and (−6,−6,−4), respectively. Slice-selection pulses were 1 ms sinc functions with two side lobes. Total TE was 18.5 ms; CHESS water suppression was turned on and off. Bottom (a–d): In vivo cat brain spectra (4.7 T, 64 scans, TR = 2 s) recorded by the above sequence without (a) and with (b) CHESS water suppression. (c) OVS-DRYSTEAM spectrum (TE = 20 ms) with water suppression during TM (50 ms) and before the sequence, showing efficient removal of most signal in the downfield region due to saturation transfer. (d) OVS–PRESS–WATERGATE spectra after cardiac arrest, showing increase in the exchangeable amide proton signals compared to (a) due to reduced exchange at lower pH. (Reproduced with permission from Ref. 1. © John Wiley & Sons Ltd., 1998)

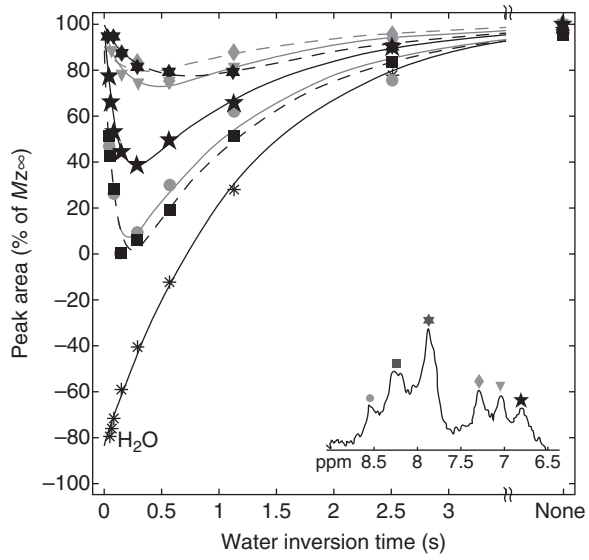

Figure 2. Inset: Downfield ^{1}H spectrum of human brain voxel (54 ml, mixed gray and white matter above the ventricles) acquired using the metabolite cycling approach without water suppression. Graph: Signal intensity (peak area averaged over 12 volunteers) for six downfield peaks (symbols indicated in inset) and water protons as a function of inversion time (TI) when adding a water ^{1}H inversion pulse before the metabolite cycling and changing TI. Peak areas are shown as a percentage of the equilibrium magnetization (determined from a 2-pool Bloch-McConnell exchange model fit) and the lines indicate the fit from the model. The fastest exchange was visible for the backbone amide proton resonances between 8 and 8.6 ppm. (Reproduced with permission from Ref. 5. © John Wiley & Sons Ltd., 2011)

As mentioned above, this spectral region consists of multiple amide proton resonances.[1–6] In order to measure the exchange rates of these protons, Macmillan *et al.*[5] performed a clever experiment in which an extra water inversion pulse was added at an inversion time TI before the metabolite inversion, and TI was then varied. Similar to the saturation contributing to apparent relaxation of solute protons explained above, every exchange of a solute proton leads to replacement by a water proton with inverted magnetization, leading to a signal reduction as a function of TI that occurs at the rate k_{sw}. The inversion slowly disappears at the rate R_1 of water (R_{1w}). The results, shown in the graphs of Figure 2, led to a k_{sw} estimate of 7–9 Hz for the 8.0–8.5 ppm resonance range, which was smaller than the average rate of about 29 Hz found in experiments on amide protons by van Zijl *et al.*[6] This was attributed to the use of a longer TE (~45 ms), which would remove several of the faster components from the spectrum because of the domination of the relaxation by the k_{sw} term. Actually, the increase in the apparent relaxation rate causes some inherent exchange rate filtering in all downfield resonances in ^{1}H MRS, in a manner dependent on the lengths of evolution periods of both longitudinal and transverse magnetizations in the particular pulse sequences. It is important to keep this in mind when trying to quantify signal intensities or exchange transfer rates.

Water Exchange (WEX) Spectroscopy

The problem of reduced or even missing signals of exchangeable protons is well known in high-resolution NMR, which has led to the use of multipulse sequences that include selective water flip-back pulses to visualize rapidly exchanging protons in multidimensional nitrogen (^{15}N)-^{1}H NMR studies of proteins.[35,39] In order to selectively detect exchanging protons and measure their exchange rates, Mori *et al.*[36,40] designed the so-called water exchange (WEX) filtered multidimensional NMR sequences that selectively label the water protons. They studied the label transfer to the amide protons and subsequently to other protons in mobile macromolecules (MM) through the intramolecular nuclear Overhauser enhancements (NOEs).[28,36,41] Analogous approaches have now been implemented in studies of perfused cells and rat brain in vivo.[6] The pulse sequences for these are shown in Figure 3(a) and (b). While the sequence for perfused cells (Figure 3a) is basically the same as for high resolution NMR with a flip-back pulse of phase (ϕ_2) opposite to the excitation pulse, the in vivo sequence (Figure 3b) requires spatially selective pulses, which complicates the use of a flip-back pulse and lengthens TE. In addition, a longer TR is needed for in vivo studies to avoid transfer of water saturation from the previous scan.

The WEX spectra (Figure 3c and d) show a wealth of information for the systems studied. In addition to the exchangeable protons of metabolites, signals are visible that can be assigned to the amide protons of mobile MMs, especially the large composite resonance around 8–8.6 ppm. Note the large amide proton resonance in the cancer cells (Figure 3c), which led to the idea of using the inverse process in amide proton transfer weighted (APTw) MRI for the detection of ischemia and cancer.[42,43]

Several important points need to be made with these spectra. First, the WEX data also provide information about

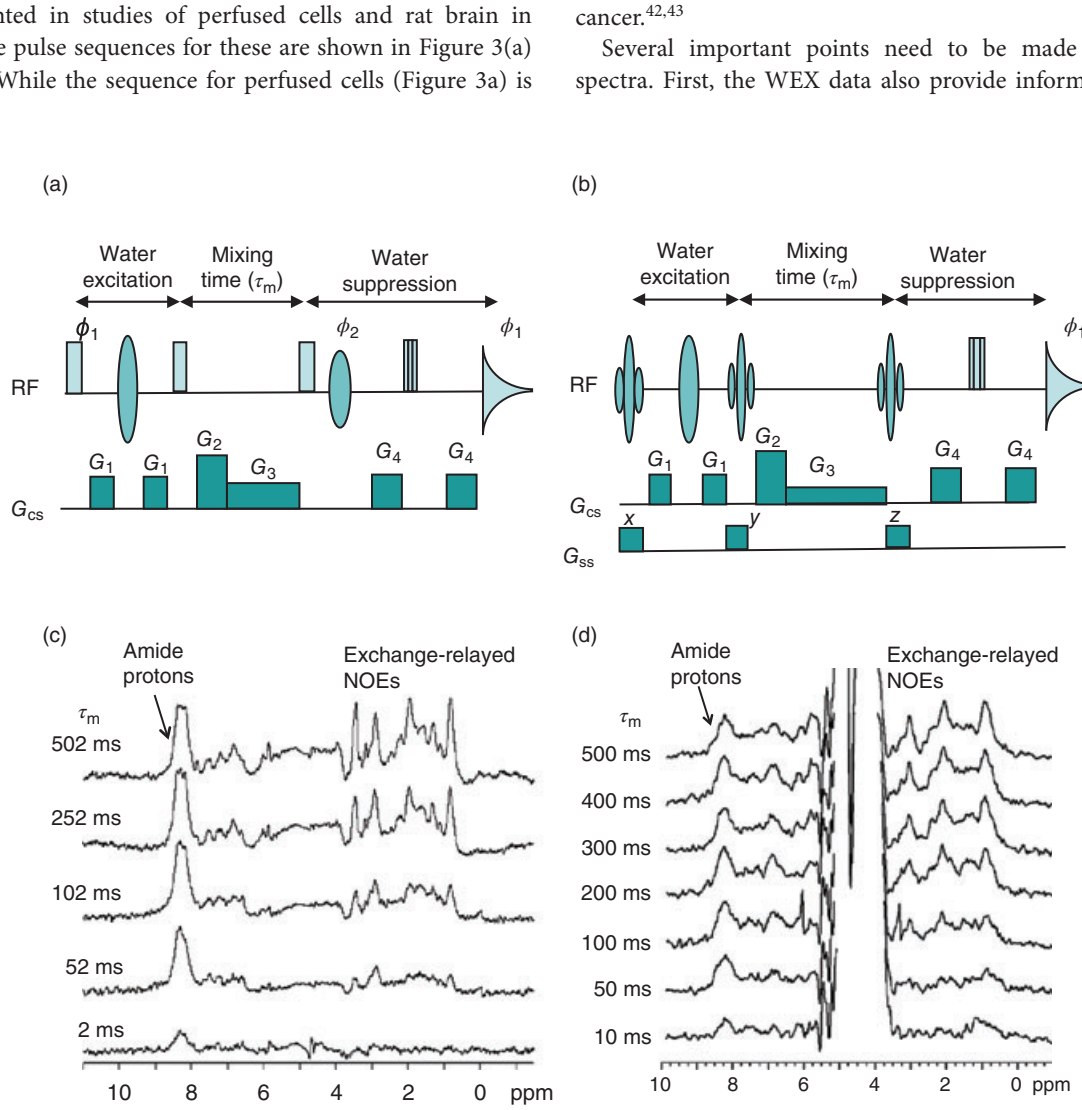

Figure 3. Water exchange (WEX) filtered pulse sequences employing hard pulse excitation with water flipback (a) and with spatial localization (b), used to acquire WEX spectra from perfused RIF-1 cancer cells at 9.4 T (c), and a cat brain in vivo at 4.7 T (d). The WEX-filtered approach uses a spin-echo based water-selective inversion pulse to label the water protons, followed by transfer to the exchangeable protons of metabolites and other molecules (such as mobile proteins and peptides) during a mixing period τ_m. Detection is done using a WATERGATE-based water-suppressed spin-echo sequence. For more details see Ref. 6. WEX spectra (c and d) show appearance of rapidly exchanging protons at short mixing time and, at later time points, exchange-relayed NOE transfer to aliphatic protons in mobile MMs. (Reproduced with permission from Ref. 6. © John Wiley & Sons Ltd., 2003)

consecutive magnetization transfer effects, such as those involving the aliphatic protons that are coupled to these amide protons, a process known from high-resolution NMR as an exchange-relayed NOE. Notice that these are intramolecular NOEs and not intermolecular NOEs to water, which would generate exchange signals of opposite phase.[44,45] Also, the spectral appearance of these aliphatic protons closely resembles that of the mobile MM signals visible in the baselines of typical proton MRS data.[6,46,47] Second, while the downfield spectra contain some very fast-exchanging protons with k_{sw} values of up to a few hundred hertz, protons with even faster exchange rates (≥1000 Hz), such as most hydroxyl and amine protons (e.g., in Glu), will be hidden in the baseline due to their large linewidths (LW = k_{sw}/π). Alternatively, at lower fields, these exchanging protons will coalesce with the water resonance if the condition of fast exchange ($k_{sw} \gg \Delta\omega$, the frequency difference with water protons) applies. Third, signals due to the magnetization transfer process from water to immobile MMs (i.e., the opposite of the MTC described by Balaban *et al.*) are also not visible because the microsecond T_2 values of these semisolid proton pools render them invisible.

Chemical Exchange Saturation Transfer (CEST)

Although they contain much information, the acquisition of WEX spectra is lengthy, which limits their practicality in the clinic. However, as Mori *et al.*[1] describing the improved detection of rapidly exchanging protons with WEX NMR, state: 'In fact, the relative intensity of solvent-exchangeable and exchange-relayed peaks to nonexchangeable peaks increases with rapid scanning because, during the short recovery period, magnetization of exchangeable peaks is replenished from the large reservoir of nonsaturated water magnetization by physical exchange, whereas nonexchanging peaks recover as a function of T_1. Without the water flipback scheme, water is saturated and recovery of magnetization at exchanging sites is determined by the T_1 of water.' This principle is actually the inverse of the CEST effect first described by Balaban and coworkers in 1990[9] and 2000,[7,8] in which exchangeable protons are detected indirectly using the water signal. This inverse approach comes with a sensitivity enhancement that allows the detection of millimolar-level metabolite signals with molar sensitivity and thus provides a potentially viable method for clinical translation. In this section, the basics of the CEST approach are described.

Principles of the Mechanism

The basic principle of CEST, as envisaged by Balaban and coworkers,[7,8] is to look indirectly at the effect of saturation of the exchangeable proton of the solute on the water signal. In conventional CEST, the spin pool of the solute protons is labeled using saturation by applying a selective RF pulse at their resonance frequency. RF-based saturation of a proton spin equalizes the spin populations of the α (spin up) and β (spin down) states, which leads to zero net magnetization of the spin pool. This process is T_1 dependent and takes time to achieve, whereas other types of saturation (e.g., excitation followed by dephasing) are more efficient. Owing to the exchange of solute protons, this saturation is transferred to the water protons, leading to partial saturation of the large pool, initially at millimolar concentrations. However, continuing exchange between the nonlabeled water pool and saturated solute protons for the duration of the saturation time (t_{sat}) leads to an accumulation of saturation and observable attenuation of the water signal (Figure 4a and b). The primary conditions for selective saturation are (i) the chemical shift of the labile proton should be sufficiently separate from that of water and (ii) the exchange rate constant should lie in the slow to intermediate range, i.e., $\Delta\omega \geq k_{sw}$.

The simplest pulse scheme for obtaining CEST data consists of a long (low-bandwidth) CW saturation pulse ($t_{sat} < 5T_1$) at a particular offset frequency, followed by any image acquisition

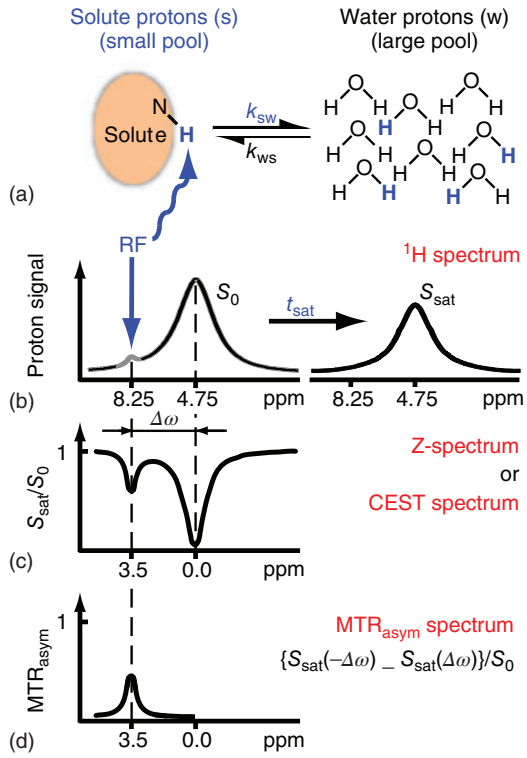

Figure 4. (a) Solute protons ('s', blue) exchange with the water protons ('w', black) with an exchange rate of k_{sw}. (b) The ^{1}H spectrum without RF saturation is indicated as S_0. The solute protons are saturated at their specific resonance frequency, which is 8.25 ppm here. This saturation is transferred to water (4.75 ppm). After a saturation period, t_{sat}, this effect becomes visible on the water signal with intensity S_{sat} (b, right). (c) The Z-spectrum, showing S_{sat}/S_0 as a function of irradiation frequency. When irradiating the water protons at 4.75 ppm, the signal disappears due to direct (water) saturation (DS). This frequency is assigned to 0 ppm in Z-spectra. At short saturation times, only this direct saturation is apparent. At longer t_{sat} the CEST effect becomes visible at the frequency of the low concentration exchangeable solute protons. (d) MTR asymmetry analysis of the Z-spectrum with respect to the water frequency to remove the effect of direct saturation. (Reproduced with permission from Ref. 21. © John Wiley & Sons Ltd., 2011)

scheme, for instance, fast spin echo,[42,43] rapid acquisition with relaxation enhancement (RARE),[48] fast imaging with steady precession (FISP),[49] or three-dimensional (3-D) gradient and spin echo (GRASE)[50] sequences. To measure CEST effects, it is common to obtain a kind of 'absorption-like' spectrum, in which images of the water signal intensity (S_{sat}) normalized with respect to signal intensity without irradiation (S_0) are acquired as a function of offset frequency (Figure 4c). These spectra reflect the loss in longitudinal magnetization and are called the Z-spectra,[51,52] or recently, CEST spectra. A significant reduction in water signal occurs after irradiation at a frequency offset that corresponds to the resonance of the CEST agent. When irradiating at the frequency of the water protons, the signal disappears because of direct water saturation (DS), an effect also known as *spillover* (Figure 4c). CEST effects can be overpowered by this DS, in particular if the solute ^{1}H resonances are close to the frequency of water.

This problem is generally addressed by analyzing the asymmetry of the Z-spectrum with respect to the water frequency (Figure 4d) to derive a magnetization transfer ratio (MTR) asymmetry factor:

$$\mathrm{MTR}_{\mathrm{asym}} = \mathrm{MTR}(\Delta\omega) - \mathrm{MTR}(-\Delta\omega) = \frac{S_{\mathrm{sat}}(-\Delta\omega) - S_{\mathrm{sat}}(\Delta\omega)}{S_0} \quad (1)$$

where $\Delta\omega$ is the shift difference between the irradiation frequency and the water frequency. For this reason, the water ^{1}H frequency is referenced as 0 ppm in a Z-spectrum, which may confuse NMR spectroscopists given that the water ^{1}H frequency is actually around 4.75 ppm. However, as in ^{1}H MRS, the convention of displaying high frequency on the left of the spectrum should be kept, which has not always been done in CEST literature. In the case of the transfer of magnetization entirely through the physical exchange of protons, as for CEST, $\mathrm{MTR}_{\mathrm{asym}}$ can be referred to as the PTR (proton transfer ratio).

The asymmetry analysis is a zero-order approach that assumes symmetrical contributions from other effects with respect to the water frequency. In practice, it is adversely affected by the presence of other asymmetrical or partially symmetrical effects. For instance, in vivo, the conventional MTC caused by the presence of semisolid structures interferes when strong RF fields are used[53–56] and the endogenous signals of multiple tissue constituents can contribute. The following sections present some methods for addressing such effects.

Analytical Equations for 'Slow' Exchange

A two-pool model of low-concentration solute protons, 's' (i.e., approximately millimolar or less), exchanging with high-concentration water protons, 'w' (~110 M), has proved satisfactory for explaining the theory of the CEST mechanism.[12,23,24,57–62] The Bloch–McConnell equation for the x, y, and z components, $M_{x,y,z}$, of the magnetization, including the effects of exchange between the water (subscript 'w') and solute (subscript 's') pools with excitation pulses applied along the x-axis, is

$$\frac{d}{dt}\begin{pmatrix} M_{xw} \\ M_{yw} \\ M_{zw} \\ M_{xs} \\ M_{ys} \\ M_{zs} \end{pmatrix} = \begin{pmatrix} -r_{2w}-\Delta\omega_w & 0 & k_{sw} & 0 & 0 \\ \Delta\omega_w & -r_{2w} & \omega_1 & 0 & k_{sw} & 0 \\ 0 & -\omega_1 & -r_{1w} & 0 & 0 & k_{sw} \\ k_{ws} & 0 & 0 & -r_{2s}-\Delta\omega_s & 0 \\ 0 & k_{ws} & 0 & \Delta\omega_s & -r_{2s} & \omega_1 \\ 0 & 0 & k_{ws} & 0 & -\omega_1 & -r_{1s} \end{pmatrix} \begin{pmatrix} M_{xw} \\ M_{yw} \\ M_{zw} \\ M_{xs} \\ M_{ys} \\ M_{zs} \end{pmatrix} + \begin{pmatrix} 0 \\ 0 \\ R_{1w}M_{0w} \\ 0 \\ 0 \\ R_{1s}M_{0w} \end{pmatrix} \quad (2)$$

with r_{1s}, k_{sw}, and r_{2s} as defined earlier, and $r_{1w} = R_{1w} + k_{ws}$, $r_{2w} = R_{2w} + k_{ws}$; M_0 is the equilibrium magnetization, $\Delta\omega_{w,s} = \omega_{w,s} - \omega_{RF}$, and k_{ws} is the exchange rate constant from the water pool to the solute pool. The relative magnitude of the exchange rates is determined by the pool sizes: $k_{sw}/k_{ws} = M_{0w}/M_{0s}$.

If the CEST experiment is performed under steady-state conditions, the derivatives on the left side of equation (2) are zero. Assuming complete saturation of the solute pool and that the RF irradiation does not perturb the water pool, then $M_{xs} = M_{ys} = M_{zs} = 0$. A simple analytical solution to the Bloch–McConnell equations with these assumptions is[24,62]

$$\frac{M_{zw}}{M_{0w}} = \frac{R_{1w}}{(R_{1w} + k_{ws})} \quad (3)$$

For a system at equilibrium, $k_{sw}M_{0s} = k_{ws}M_{0w}$, equation (3) can be rearranged as

$$\frac{M_{zw}}{M_{0w}} = \frac{R_{1w}}{(R_{1w} + k_{sw}(M_{0s}/M_{0w}))} \quad (4)$$

Similarly, for a transient system, i.e., when the state of the system changes with time, for $t_{sat} < T_1$, and assuming that there is no spillover effect on water pool, the steady state (s-s) solution of equation (2) becomes

$$\frac{M_{zw}}{M_{zw}^{s-s}} = \frac{k_{sw}(1 - e^{-r_{1w}t_{sat}})}{r_{1w}} \quad (5)$$

For incomplete saturation of the exchanging proton, using $M_{zw}^{s-s} = \alpha M_{0w}$ and $\mathrm{PTR} = 1 - M_{zw}/M_{0w}$, we find

$$\mathrm{PTR} = \frac{x_s\alpha k_{sw}\left(1 - e^{-(R_{1w}+k_{ws})t_{sat}}\right)}{R_{1w} + k_{ws}} \quad (6)$$

where α is the saturation efficiency of the proton pool being irradiated and x_s is the concentration ratio of the exchangeable proton pool:

$$\alpha \approx \frac{(\gamma B_1)^2}{(\gamma B_1)^2 + (k_{sw})^2} \quad (7)$$

$$x_s = \frac{[\text{exchangeable proton}]}{[\text{water proton}]} = \frac{k_{ws}}{k_{sw}} \quad (8)$$

Thus, PTR increases with the exchangeable proton concentration, the exchange rate constant, and the efficiency of the saturation applied to the exchangeable protons. For greater saturation efficiency, a saturation pulse with a higher power

would be required, but that may have disadvantages in vivo because of increased DS and MTC interference. Moreover, RF power is generally limited by the scanner RF duty cycle. Exceeding the allowed tissue-specific absorption rates (SAR) in vivo is also a concern, but in most practical situations on 3 T clinical scanners with body coil excitation or 7 T scanners with head transmit, the RF duty cycle limits are reached well before the SAR limit. Notice that saturation can never be more than 100%. Thus, at a higher concentration of protons or at very high exchange rates with efficient saturation, PTR is no longer proportional to concentration. This is accounted for by the exponential term in equation (6), and the water–solute exchange term (called back-exchange in the CEST literature) in the denominator. The dependency of PTR on the exchange properties and concentration of contrast agents makes CEST MRI a valuable tool to probe tissue properties.

Selective saturation of the solute without affecting the water pool requires the second primary condition (a slow to intermediate exchange rate, $\Delta\omega \geq k_{sw}$, see section titled 'Principles of the Mechanism'). Thus, a high magnetic field (B_0) offers an advantage for CEST measurements, as the chemical shift difference between water and the agent being irradiated increases linearly with B_0. The SNR for water also increases approximately in proportion to B_0, offering higher spatial resolution and a decrease in the imaging time compared to low field. Last but not least, T_{1w} increases with B_0, which allows the label to stay around longer.

Relayed Nuclear Overhauser Enhancement (rNOE)

While we focused in the previous sections on the propensity of exchangeable protons to transfer magnetization, dipolar interactions within or between molecules can provide an alternative transfer pathway. Saturating or exciting (e.g., with an inversion pulse) a spin population of protons A in a molecule will affect the population of nearby protons B, if A and B have sufficient dipolar through-space coupling to relax each other (via a T_1 effect). This is the NOE effect, which depends on the distance between the protons. It is small and positive for smaller molecules with rotational diffusion in the extreme narrowing limit (long T_2s), and increases and becomes negative for larger molecules. Such dipolar transfer is greatest in immobile MMs where fast cross-relaxation occurs rapidly over large spin systems, an effect known as *spin diffusion*. This is the case for the semisolid cell structures detected in the MTC effect, where such magnetization can be further transferred to the solvent via intermolecular dipolar interactions between bound water molecules that exchange with free water[12,23,57–59,62–66] or via exchanging protons.[67]

The first report of NOE effects in CEST spectra was in the work of Ling *et al.*[68] on glycosaminoglycan (gag) in bovine patella (Figure 5). The gag signals upfield from water were assigned to residues contributing via intermolecular NOEs to water, but this is an unlikely origin given previous high-resolution NMR studies of mobile MMs. For MMs with sufficient mobility to have visible NMR signals, such as gag, proteins, and peptides in plasma, the direct intermolecular interaction to bound water is known to be too weak[44,45] and the NOE-relayed (rNOE) exchange mechanism dominates.[21,69]

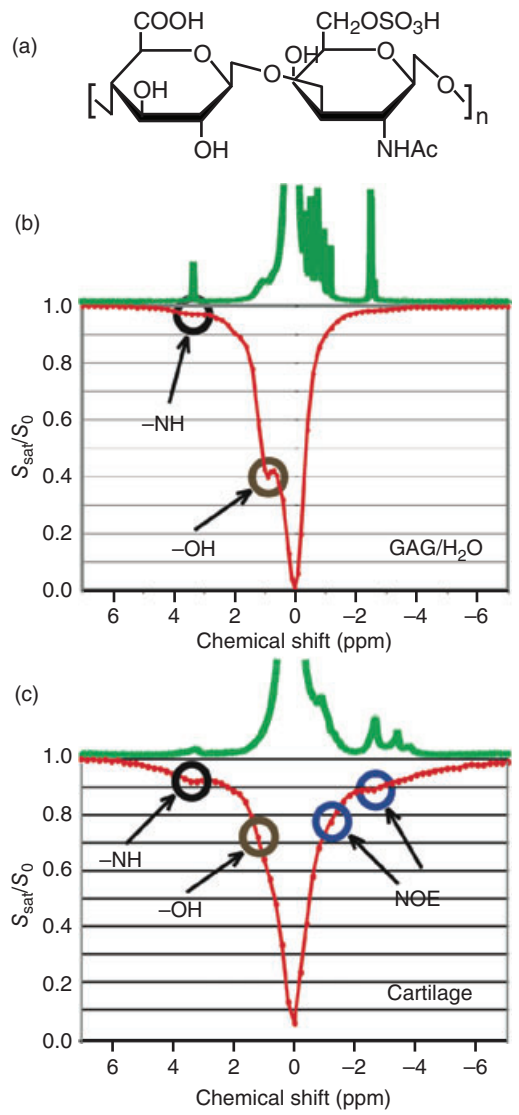

Figure 5. (a) Structure of a gag-unit showing three OH groups, an amide proton, and several aliphatic protons in the ring (CH) and the *N*-Acetyl side chain. (b) Z-spectra of 125 mM gag units in solution, showing predominantly NH and OH exchange saturation transfer effects. (c) Z-spectra of cartilage from bovine patella in PBS (phosphate-buffered saline) showing exchange and much increased NOE effects. (Reproduced with permission from W. Ling, R. R. Regatte, G. Navon and A. Jerschow, Proc Natl Acad Sci U S A, 2008, 105, 2266. © 2008, National Academy of Sciences, U.S.A.)

This is the reverse of the exchange-relayed NOEs measured in the WEX spectra (Figure 3). rNOE effects on mobile molecules have further been detected in the brain in animals[70] and humans.[71] However, they are difficult to detect without interference with the MTC effect, which is of course also NOE based. Only at very low B_1 field does the fine structure of the mobile components become visible above a broader MTC residual.[72] Recent data[73] using a pulse sequence that can remove the MTC component have confirmed that these rNOE-CEST effects in the brain are of equivalent magnitude in gray matter (GM) and white matter (WM), while the myelin-based MTC is dominant for WM. Evidence from the WEX spectra indicate that the

rNOE effects originate from the mobile MM baseline in ^{1}H MRS. Recent MRS data show mobile MM concentrations to be of comparable magnitude in WM and GM,[74] supporting this assignment of the CEST-based NOE effects.

In Vivo CEST Spectrum

The purpose of asymmetry analysis is the removal of interfering contributions, which are assumed to be symmetrical about the water signal in the Z-spectrum. While this is effective for removing direct saturation effects in most in vitro cases, it fails in vivo due to the presence of exchangeable protons from other tissue metabolites, rNOEs of mobile MMs, and intermolecular NOEs and rNOEs from semisolid tissue components. The MTR_{asym} defined in equation (1) reflects these other effects too:

$$MTR_{asym}(\Delta\omega) = MTR_{asym}^{CEST}(\Delta\omega) + MTR_{asym}^{MTC}(\Delta\omega) + MTR_{asym}^{rNOE}(\Delta\omega) \quad (9)$$

where superscripts CEST, MTC, and rNOE refer to the MTR asymmetries measured as arising from those respective causes. Thus, both long and short T_2 spin systems and slow and fast transferring components contribute to the MTR_{asym}, the relative magnitude of which depends on the B_1 field used.[53,69,75] At low B_1, slow exchanging protons (<100 Hz, mainly amide protons) and rNOEs from mobile MMs dominate. As B_1 is increased, the comparatively faster exchanging amide, amine, imino, and hydroxyl protons and the partially asymmetric conventional MTC effect become dominant. Direct saturation also becomes prominent with stronger saturation. Depending on the B_1 and pulse sequences used for saturation, there is an ongoing development effort to design approaches for removing some of the interfering components. A few of these approaches are discussed next.

Pulse Sequences for MTC and CEST MRI

The sensitivity of magnetization transfer MRI to multiple mechanisms and to pulse sequence parameters complicates comparison of studies between laboratories. This has been a hurdle for clinical trials using MTC as a biomarker for myelin, and will no doubt also affect such efforts for CEST studies. CEST has been around for 15 years and most approaches are similar to methods previously developed for the study of MTC, i.e., the use of CW or pulsed saturation. As such, it often seems that saturation labeling is the only approach available and that CEST methods will have the same issues as MTC approaches. However, this is not the case. CEST MRI has many more possibilities than MTC MRI because of the different T_2 properties of the protons studied in CEST MRI compared to the semisolid protons detected in MTC ($T_{2liquid} \gg T_{2solid}$). This enables the use of spectroscopic techniques for signal editing that will not work for MTC, and provides opportunities to separate exchange transfer effects from MTC and DS effects. Specifically, while MTC components dephase within tens of microseconds, the longer T_2s in CEST can be exploited in pulse sequences with varying time delays between the excitation pulse components. Such time delays can be used to encode protons during evolution of the transverse magnetization (frequency encoding) or during periods of longitudinal magnetization recovery and transfer (transfer rate encoding/filtering). This allows the editing of individual proton types and the use of a powerful array of multidimensional FT NMR methods for detection, analysis, and quantification of CEST agents. In the following sections, the saturation pulse sequences used for MTC and CEST MRI are first summarized, followed by an overview of several pulse sequences for editing exchangeable magnetization components.

Saturation-based Pulse Sequences

CEST labeling is very similar to MTC labeling in that any pulse sequence that sensitizes the bulk water pool to magnetization transfer from a small pool can be used to measure the presence of such a pool. For MTC, this has led to a large range of approaches for water saturation (for some reviews, see Refs 63–65, 76, 77) employing multiple mechanisms using both on-resonance and off-resonance water saturation. A pulse sequence overview including most of the MTC preparation schemes is shown in Figure 6. These schemes can be separated into CW off-resonance (Figure 6a), and pulsed multistep on- or off-resonance (Figure 6b and c) approaches. In the classical CW saturation, a long (t_{prep} = several seconds) low-power RF irradiation is used during which partial saturation [see equation (7)] is transferred continuously to bulk water (Figure 6a). Alternatively, one can apply frequency-selective off-resonance pulsed saturation using a series of frequency-selective pulses of higher B_1 amplitude and of medium length (t_{sat} of order 1–50 ms, depending on coil size and available RF power) spaced by millisecond time intervals (t_{delay}; Figure 6b). The pulses are repeated continuously to build up and maintain a steady-state saturation.[77–84] This can be done in a multistep preparation as well as by single steps between image acquisitions when using fast MRI (the pulsed steady-state approach).

A second version of the multistep approach for reducing the water signal through MTC is to use multistep on-resonance 'saturation' (Figure 6c).[82] The quotation marks are added to stress that this is not true saturation in the classical sense of population equilibration, but a randomization of the magnetization through dephasing. In the imaging literature, this definition of saturation, e.g., through the use of gradient dephasing, is common. In these on-resonance approaches the free bulk water pool is quickly excited relative to its T_2* with millisecond pulses or faster, and returned to equilibrium (e.g., using two 90° pulses of opposite sign or two 180° pulses of the same or opposite sign), without being affected much. The semisolid proton pool, however, has a T_2* (and T_2) on the order of microseconds, and rapidly loses coherence due to random dephasing. Consequently, it loses longitudinal magnetization after each excitation flip-back step. Saturation of the bulk water then builds, due to transfer, and is increased using a series of pulses. The inherent beauty of this scheme is that it has a high 'saturation' efficiency for the semisolid macromolecule pool since all excited spins are dephased within microseconds. In addition, high B_1 can be applied to obtain a large saturation bandwidth. It should be noted that the pulsed scheme is a

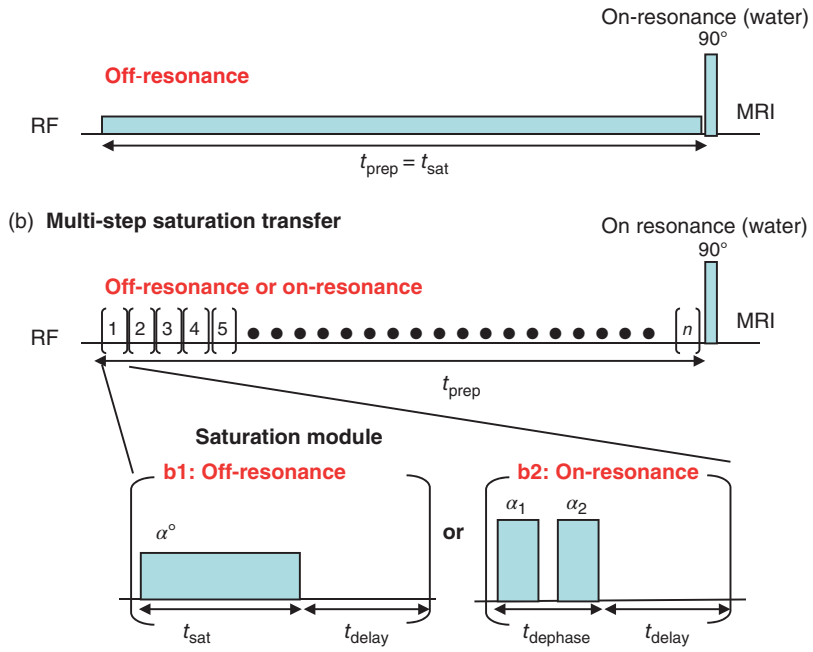

Figure 6. (a and b) Pulse sequences with preparation schemes for MTC saturation transfer, slightly modified to also allow some additional CEST editing. During the preparation time (t_{prep}), one can use (a) CW selective saturation at a specific frequency; (b) 'multistep' saturation transfer, in which partial saturation is accomplished in each step (module). Saturation modules, [n], containing pulses of length $t_{sat,}$ are repeated during $t_{prep} = n \cdot (t_{sat} + t_{delay})$, slowly increasing the saturation of water. For the off-resonance module, a selective pulse of reduced B_1 is applied. Repetition during the sequence builds up a saturation steady state. For the on-resonance module (water frequency): short pulses of high B_1 (hard pulses) are applied to rotate the water magnetization quickly to ($\alpha_1 = 90°$) or through ($\alpha_1 = 180°$) the transverse plane, and back to the z-axis ($\alpha_2 = -90°$ or $\pm 180°$). The water proton magnetization is not affected while the semisolid macromolecular proton magnetization is efficiently dephased, leading to longitudinal signal loss after exchange. (c) Steady-state pulsed MT with acquisition after each pulse with low flip angle β, typical for gradient-echo acquisition

kind of hybrid approach as it has both classical saturation and dephasing contributions.

A third type of MTC scheme has been suggested by Gochberg and Gore,[85,86] which is to apply a non-selective single inversion pulse, followed by monitoring of the biexponential recovery of the bulk water pool signal, and the effect due to its interaction with the semisolid pool.

Intuition indicates that CEST effects should be detectable in a manner similar to MTC effects, and most of the early CEST work used the classical CW off-resonance selective-saturation approach to acquire Z-spectra or partial Z-spectra followed by an MTR asymmetry analysis. However, some studies have employed pulsed selective saturation using a series of pulses during t_{prep} [42,43,87,88] or pulsed steady-state approaches.[71,72] Vinogradov *et al.*[89,90] have shown that the presence of micromolar concentrations of paramagnetic CEST (PARACEST) agents can be detected using an on-resonance pulse scheme in which water signal is continuously undergoing 360° rotations using a so-called 'WALTZ' multipulse scheme compensated for B_1-inhomogeneity. It is important to note that this latter approach differs from on-resonance MTC schemes in that the small solute pool is not excited. During a series of such pulses, the water signal is reduced due to magnetization leakage from bulk water to the contrast agent, so that part of the magnetization does not experience full 360° pulses. As such, this is a new type of sequence that selectively detects rapidly exchanging protons. However, there will still be interference from the MTC background unless the sequence is applied dynamically during the infusion of the CEST contrast agent. Dynamic studies allow selective detection of the agent by studying the signal intensity change as a function of time. This sequence was called 'OPARACHEE' (On-resonance PARamangnetic Chemical Exchange Effects), as it was first applied to paraCEST agents that had very fast exchange rates (often tens of thousands hertz)

of water protons at their coordination sites. It could be used for fast exchanging protons in diamagnetic CEST (diaCEST) agents too, if their excitation could be avoided, although that may be difficult when they are close to the water ^{1}H resonance.

Because of the use of very similar, if not equivalent, pulse sequences for MTC and early CEST studies, in vivo CEST data analyzed using MTR_{asym} [see equations (1) and (9)] are generally contaminated by asymmetric MTC effects. Actually, even if MTC effects were symmetric, these two mechanisms generally cannot be added in a zero-order approach but are interdependent, especially at higher B_1.[53] Recent efforts have therefore focused on trying to separate out MTC and CEST effects using sequences that exploit the different properties mentioned above. In particular, the difference in the R_2 of the protons involved leads to fast incoherent dephasing in the MTC pool but an identifiable resonance in the CEST and rNOE signals from mobile species. A second property that distinguishes MTC from CEST is that dipolar through-space interactions are not affected by pH, while chemical exchange is pH dependent (albeit not measurable if the exchange is very fast). However, pH is quite stable in vivo (except in some pathologies such as ischemia) and differs in tumors which thus may be more sensitive to CEST. Approaches for editing MTC effects based on saturation (see section titled 'Saturation-based Editing Sequences') and excitation (see section titled 'Exchange Transfer Sequences Employing Excitation') are discussed next.

Saturation-based Editing Sequences

Editing for the purpose of separating out multiple magnetization transfer mechanisms can be achieved by appropriately modulating B_1, frequency offset, saturation time and/or the interpulse delay in the sequences shown in Figure 6. The simplest way to minimize MTC effects in CEST studies is by using a very low B_1-field. This can be done using the steady-state pulsed approach in Figure 6(c). A typical steady-state Z-spectrum is displayed in Figure 7(b). When subtracting the DS using a Lorentzian difference (LD) fit (see section titled 'Data Analysis for CEST Spectra'), the spectrum at negative frequency shows the narrow rNOE contributions on top of a small broad asymmetric MTC effect (Figure 7c and d). The resulting images therefore still highlight WM (Figure 7e), and more advanced editing is needed to obtain clean rNOEs and other CEST effects.

Equations (10a)–(10d) define several more intricate acquisition schemes that use frequency-offset modulation, saturation-time modulation, or interpulse-delay time modulation to separate MTC and CEST effects. Note that all schemes acquire an extra S_0 scan without saturation, and that several, but not all, acquire a B_0 map for correcting center frequency in the Z-spectrum:

$$\text{SAFARI}\ [S_1, S_2, S_3, S_4] = [S(\Delta\omega), S(\Delta\omega, -\Delta\omega), S(-\Delta\omega), S(-\Delta\omega, \Delta\omega)] \quad (10a)$$

$$\text{LOVARS}\ [S_1, S_2, S_3, S_4] = [S(-\Delta\omega, t_{sat1}), S(-\Delta\omega, t_{sat2}), S(+\Delta\omega, t_{sat1}), S(+\Delta\omega, t_{sat2})] \quad (10b)$$

$$\text{meLOVARS} \begin{bmatrix} S_1, S_2, S_3, S_4 \\ S_5, S_6, S_7, S_8 \end{bmatrix} = \begin{bmatrix} S_1(-\Delta\omega, t_{sat1}), S_2(-\Delta\omega, t_{sat2}), S_3(-\Delta\omega, t_{sat3}), S_4(-\Delta\omega, t_{sat4}) \\ S_1(+\Delta\omega, t_{sat1}), S_2(+\Delta\omega, t_{sat2}), S_3(+\Delta\omega, t_{sat3}), S_4(+\Delta\omega, t_{sat4}) \end{bmatrix} \quad (10c)$$

$$\text{VDMP}\ [S_1, S_2, S_3, \ldots\ \ldots\ \ldots] = [S_1(\Delta\omega, t_{delay1}), S_2(\Delta\omega, t_{delay2}), S_3(\Delta\omega, t_{delay3}), \ldots\ \ldots\ \ldots] \quad (10d)$$

The nomenclature for these methods is defined in the subsections below.

SAFARI. The SAFARI (saturation with frequency alternating RF irradiation) approach[91] was designed to detect exchangeable protons with a slow exchange rate (<100 Hz) that can be rapidly saturated with low B_1 [according to equation (7)], the best example being amide protons in amide proton transfer (APT) studies. It employs four acquisitions consisting of two steps with alternating $\pm\Delta\omega$ frequency irradiation relative to the water resonance frequency in a series of multiple saturation pulses (Figure 6b1), intermixed with control scans at the actual positive and negative frequencies. Subtraction of the control scans from the two alternating scans removes the DS and asymmetric MTC effects and is insensitive to B_0-inhomogeneity as long as the saturation bandwidth is large enough to always hit a main section of the exchangeable proton resonance. It appears that all effects including CEST should be cancelled in the subtraction, but the presumption in the SAFARI method is that the saturation for amide protons is achieved rapidly while that for the DS and MTC effects keeps increasing with the number of pulses. Under that condition, the dual-frequency steps would each give a CEST effect equivalent to the single positive frequency irradiation. One can then calculate a new MTR parameter that is equivalent to the PTR in equation (6):

$$\begin{aligned} MTR_{SAFARI} = &[2S_0 - S(\Delta\omega, -\Delta\omega) - S(-\Delta\omega, \Delta\omega) - S_0 \\ &+ S(\Delta\omega) - S_0 + S(-\Delta\omega)]/S_0 = 2PTR \\ &+ DS(\Delta\omega) + DS(-\Delta\omega) + MTC(\Delta\omega) \\ &+ MTC(-\Delta\omega) - PTR - DS(\Delta\omega) - DS(-\Delta\omega) \\ &- MTC(\Delta\omega) - MTC(-\Delta\omega) = PTR \end{aligned} \quad (11)$$

Unfortunately, there are two issues with this approach. First, although the asymmetric MTC is suppressed for homogeneously broadened semisolid components, this is not the case for inhomogeneously broadened structures such as membranes. Actually, using higher B_1 and larger offsets, this dual frequency difference approach has recently been used to detect myelin-containing membranes.[92] Second, in addition to amide protons, aliphatic protons in mobile molecules are also labeled and this slow-transferring label is also retained in the MTR_{SAFARI}. The relative contributions of these APT and rNOE effects depend not only on the number of pulses but also change with the inter-pulse delay, complicating the interpretation of the SAFARI data.

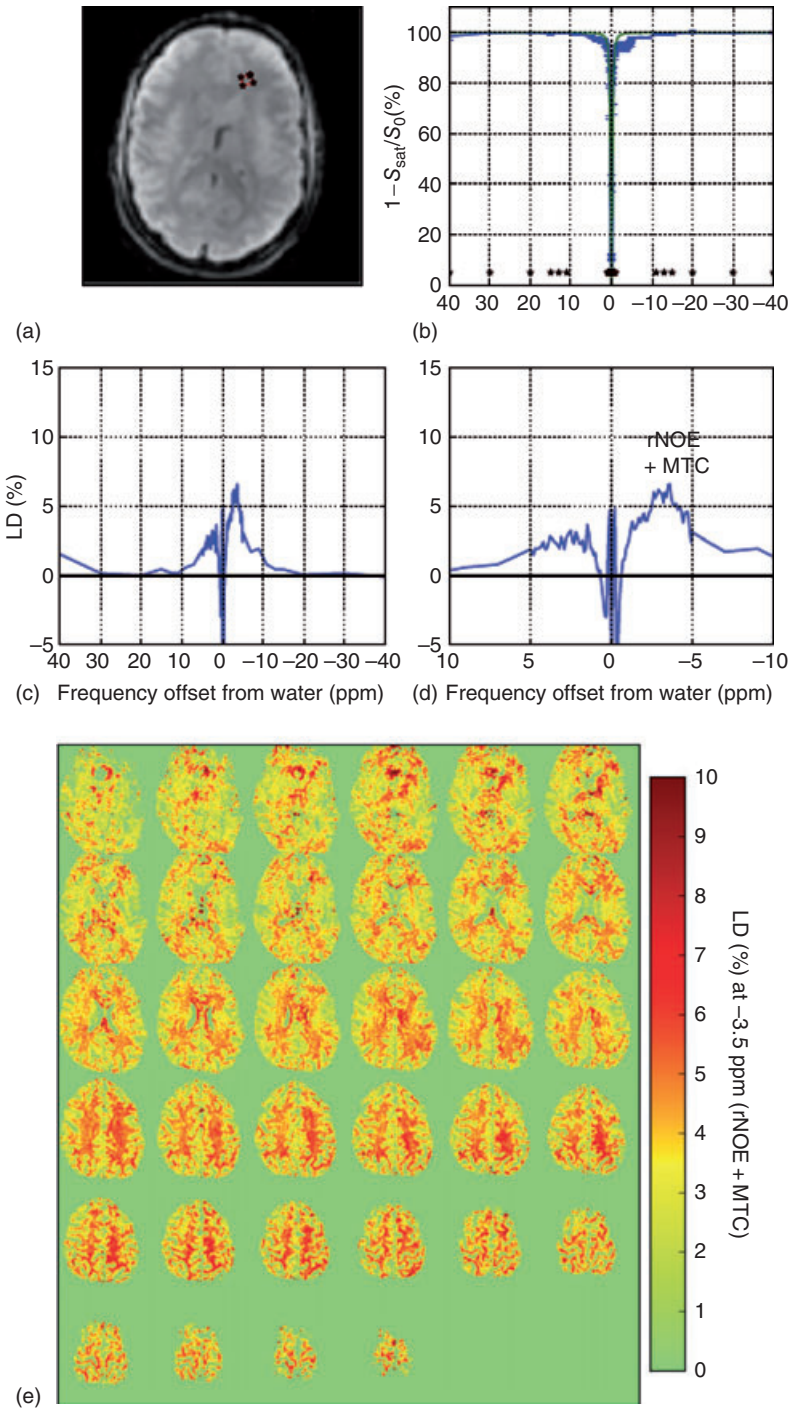

Figure 7. Results from pulsed steady-state saturation experiments with $B_1 = 1\,\mu T$ and 25 ms pulses. (a) Axial unsaturated image and ROI. (b) Z-spectrum and Lorentzian fit (green line) of the direct water saturation contribution based on fitting the frequency offsets (shown as stars, bottom) for a region of white matter. (c) Lorentzian difference (LD) spectrum (40 to −40 ppm) for the white matter region, defined as the difference between the Lorentzian fit and the acquired Z-spectrum. (d) LD spectrum zoomed in to show the 10 to −10 ppm region. Steady-state pulsed CEST acquisition showing both CEST effects (at positive frequencies) and rNOE signals (negative frequencies) on top of a broad and asymmetric MTC background. (e) LD images at −3.5 ppm, showing white matter highlighted due to the MTC contributions to the LD. Later studies have shown rNOE to be equal between white and gray matter when MTC is removed properly (Figure 9). (a-d are reprinted from Neuroimage, 77, C. K. Jones, A. Huang, J. Xu, R. A. Edden, M. Schar, J. Hua, N. Oskolkov, D. Zaca, J. Zhou, M. T. McMahon, J. J. Pillai and P. C. van Zijl, Nuclear Overhauser enhancement (NOE) imaging in the human brain at 7 T, 114. © 2013, with permission from Elsevier[72]; (e) is from the same dataset, but not previously published)

Other groups have studied the use of dual frequency irradiation. For instance, Narvainen *et al.*[93] reported an approach using Z-spectroscopy with alternating phase irradiation (ZAPI). This method exploits the T_2-selectivity of the irradiation pulse to differentiate the various contributions to a Z-spectrum. By using phase modulation (every 100 μs) of a low-power continuous saturation pulse, the short-T_2 MTC components are selectively saturated through random dephasing, while sidebands are generated at the frequencies of long-T_2 components. Owing to the fact that a low B_1 is used, the method is relatively insensitive to fast exchanging solute molecules and mainly reveals the MTC components. The selection of long-T_2 components using this approach needs to be further developed. Lee *et al.*[94,95] provided a theoretical description for such dual-frequency saturation either with alternating pulses of opposite frequency (SAFARI-like) or phase-modulated CW irradiation (ZAPI-like). They demonstrated that the MTC asymmetry can be reduced through such alternating saturation, because

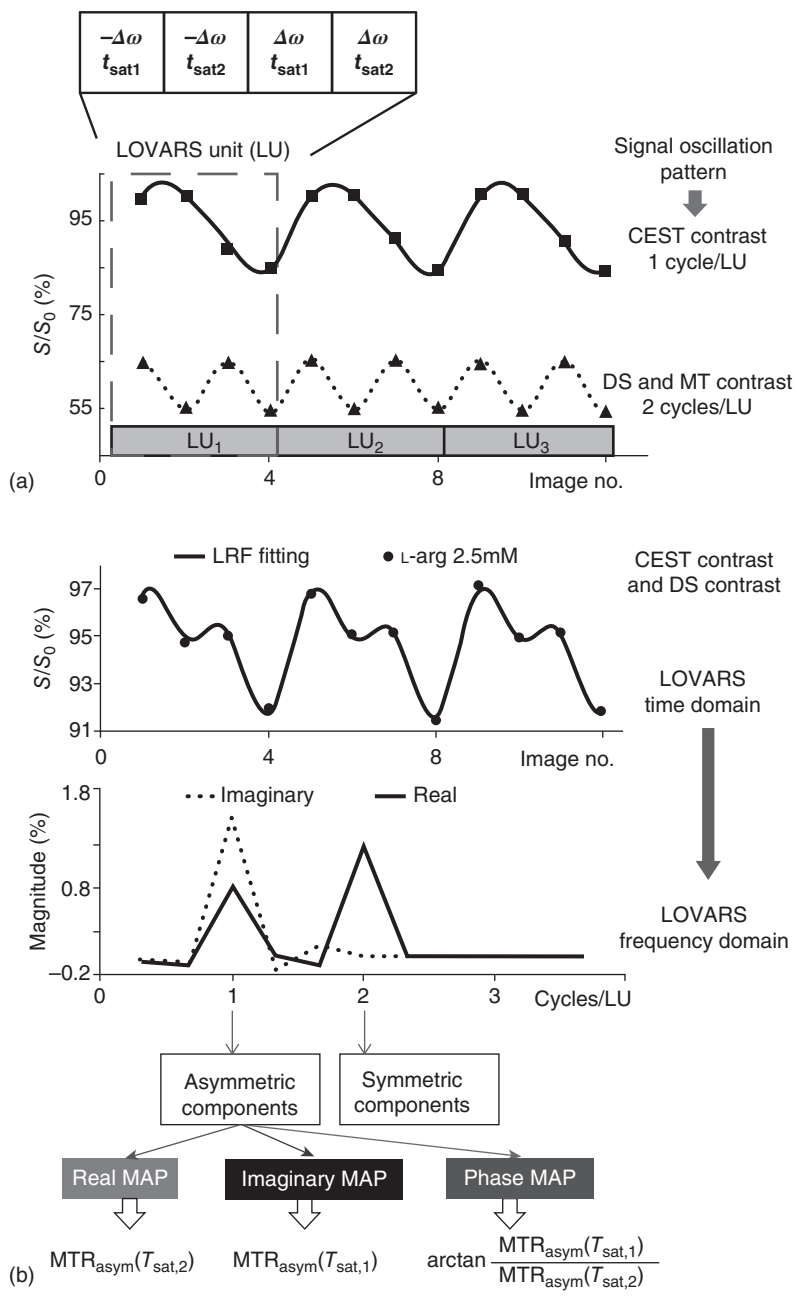

Figure 8. Illustration of the LOVARS signal response for the sequence in equation (10b). Three LUs are displayed. (a) The resulting signal patterns produced on either 5 mg/ml poly L-lysine (upper, solid squares, $\Delta\omega = 3.5$ ppm) or 4% agar (lower, solid triangles) with the data fit to the general LOVARS equation for the modulation. CEST contrast oscillates at 1 cycle/LU and DS and MTC oscillates at 2 cycles/LU. (b) The LOVARS signal modulation for L-arginine (2.5 mM), $\Delta\omega = 1.8$ ppm, containing both CEST and DS contrast. Transformation to the LOVARS frequency domain generates the LOVARS parameters for each voxel: real, imaginary, and phase values. (Reproduced with permission from Ref. 96. © John Wiley & Sons Ltd., 2012)

strongly coupled spin systems are saturated uniformly if the saturation is much faster than the exchange, which is the case for the microsecond T_2s of solid-like structures. The CEST effects were still well distinguished at the sideband frequencies for MTR asymmetry analysis.

LOVARS and meLOVARS. The LOVARS ('length- and offset-varied saturation') approach[96] has a four-part acquisition with $\Delta\omega$ and t_{sat} varied to induce different modulations in the saturation-transfer contrast for CEST versus DS and MTC. This simple and ingenious principle is demonstrated on phantoms in Figure 8 using a series of 2–3 of the LOVARS units (LUs) as shown in equation (10b). For DS and MTC in a solution of 4% agarose, saturating at $\pm\Delta\omega$ gives the same effect (i.e., symmetric components), while an increase in t_{sat} ($t_{sat2} > t_{sat1}$) leads to increased saturation. Thus for the LU in equation (10b), where t_{sat} is varied twice, one gets two modulations per unit (Figure 8a). For a CEST agent (5 mg/ml polylysine, $\Delta\omega = 3.5$ ppm) there is a small saturation at -3.5 ppm where only limited DS occurs, but a large effect at the positive frequency (limited DS + CEST) for this asymmetric component. Only a small t_{sat} dependence is found, because full saturation is easily achieved for these amide protons (Figure 8a). When using a solution of L-arginine (amine protons at $\Delta\omega = 1.8$ ppm), there is DS saturation dependence at $-\Delta\omega$ and a (DS + CEST) dependence at $\Delta\omega$.

After Fourier transforming this so-called LOVARS response function (S_{LRF}), the asymmetric component can be separated out to obtain MTR_{asym} for the two saturation times as real and imaginary data (Figure 8b). Despite the simplifying assumption of symmetric MTC, the approach was applied successfully in vivo for imaging APT effects, but may have some contamination by MTC. The contrast-to-noise ratio (CNR) was about three to four times that of conventional CEST with the same imaging time, taking into account the extra acquisition time required for conventional CEST (to acquire data for the B_0 correction).

In order to speed up the acquisition, Song *et al.*[97] also designed the meLOVARS (multi-echo length- and offset-varied saturation) approach that divides the saturation preparation time into three to eight modules of equal length [four shown in equation (10c)], each followed by a multi-echo acquisition. Since the effect of the sequence applications is cumulative, the method depicted by equation (10c) leads to data that measures the effect at four different saturation times of increasing length ($t_{sat2} = 2t_{sat}$; $t_{sat3} = 3t_{sat}$ and $t_{sat4} = 4t_{sat}$) within one LU. This allows investigators to determinate exchange rates similar to the QUEST (quantifying exchange using saturation time) approach of McMahon *et al.*[98] Successful in vivo experiments showed improved CNR compared to LOVARS in reduced time.

VDMP. The VDMP (variable-delay multi-pulse) approach of Xu *et al.*[69] exploits the differences in transfer time between different mechanisms to select out the ones of interest. Figure 9(a) shows this principle based on Bloch simulations for MTC, rNOE, amide protons, and amine protons for the pulse sequence in Figure 6(b1) with 16 RF pulses and multiple delay times. Fast-exchanging protons such as amines only saturate during the magnetization transfer pulse, and the signal reduces relative to $t_{delay} = 0$ ms. MTC and CEST saturation occur only during the pulses, but it is transferred slowly and the effect increases with delay time based on the transfer rate before reducing with T_{1w}. The variation of DS with t_{delay} is small as T_{1w} is on the order of a second. By choosing a t_{delay} at which MTC effects are equal, a VDMP difference spectrum can be calculated that removes MTC and DS effects independent of any asymmetry. This is illustrated in Figure 9(b) and (c) for human brain at 7 T,[73] and allows pure APT and NOE effects to be calculated. Note that the rNOE effects are equal for WM and GM, consistent with results for the mobile MM baseline from MRS studies.[74]

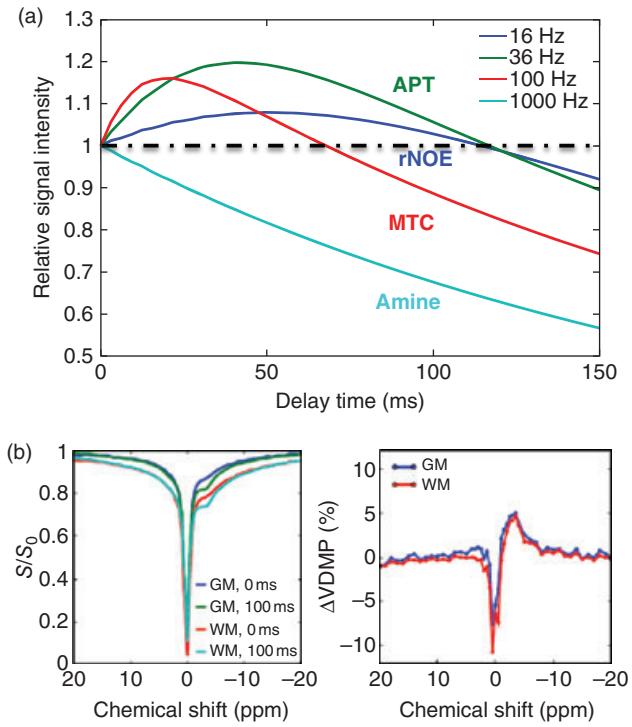

Figure 9. Illustration of the variable delay multi-pulse (VDMP) sequence parameters and results. (a) Bloch simulation of delay time-dependent signal intensity ratio for magnetization transfer at different rates. The signal intensity ratio is normalized to CEST intensity at $t_{delay} = 0$ ms. Signal builds up with the transfer rate and reduces with T_{1w}, with a profile that depends on the relative rate. Rapidly exchanging amine protons (1000 Hz) transfer instantly and increasing t_{delay} only reduces the CEST effect, while MTC first increases and then decays similar to the even slower amide (APT) and relayed NOE (rNOE) effects. The simulation was performed assuming 16 RF pulses (10 ms, 2 μT). (b) Z-spectra of human white matter (WM) and gray matter (GM) at 7 T, acquired using $\tau_{delay} = 0$ and 100 ms, where the MTC effect is about equal. (c) The corresponding VDMP difference spectra for WM and GM. (Reproduced with permission from John Wiley & Sons Ltd. © 2015)

Several other saturation-based sequences are being developed. One of interest is a recent method in which a positive CEST ('pCEST') signal is obtained[99] by placing an inversion pulse before the CW sequence in Figure 6(a). For $B_1 = 0$, the signal can be nulled using an appropriate inversion delay, while adding saturation causes an apparent increase in the relaxation and thus a positive signal.

Exchange Transfer Sequences Employing Excitation

The previous sections showed that sequences used for MTC detection can also be used for CEST MRI, i.e., CW or pulsed RF saturation with variable saturation times and B_1. It also demonstrated that additional sequences can be designed to separate MTC and CEST longitudinal magnetization, for instance, by varying the delay (t_{delay}, also called t_{mix}) between saturation pulses. However, the fact that CEST and rNOE data are from long-T_2 components permits the design of novel editing principles using excitation (rotation) of the magnetization and evolution of the transverse magnetization. Two things have to be remembered. First, any sequence using hard RF pulses will lead to saturation of MTC components and spillover to the water signal. We will see that these contributions can be edited out. Second, a single excitation allows detection only at the concentration of the CEST agent, so the excitation sequence has to be repeated. Caution is therefore required when these ideas are applied in vivo, because repetition of high-B_1 pulses needs to be kept within safety guidelines for SAR and RF hardware constraints.

Inversion and Dephasing Transfer. The general pulse sequence, illustrated in Figure 10, resembles the pulsed-MTC sequence in Figure 6(b) but has different elements dubbed 'Label Transfer Modules' (LTMs[21,100]). The exchangeable proton spins are magnetically labeled by the LTMs, either using excitation or offset-frequency-sensitive evolution of transverse magnetization, after which this label is transferred to the water protons. This principle allows several new labeling types to be used, including selective inversion (Figure 10a), excitation and dephasing (Figure 10b), rotation-angle encoding (Figure 10c), delay time encoding (Figure 10d), and frequency encoding (Figure 10e). In the inversion approach, the transferred Z-magnetization is of opposite sign to the equilibrium water magnetization. Consequently, this approach is twice as efficient as CW or dephasing saturation in which zero magnetization is transferred. Note that this is not the case when using inversion pulses for MTC, because the magnetization will be dephased instead of inverted, due to the short T_2*. The inversion transfer and dephasing transfer are normally applied as frequency-selective pulses, and CEST signals will thus

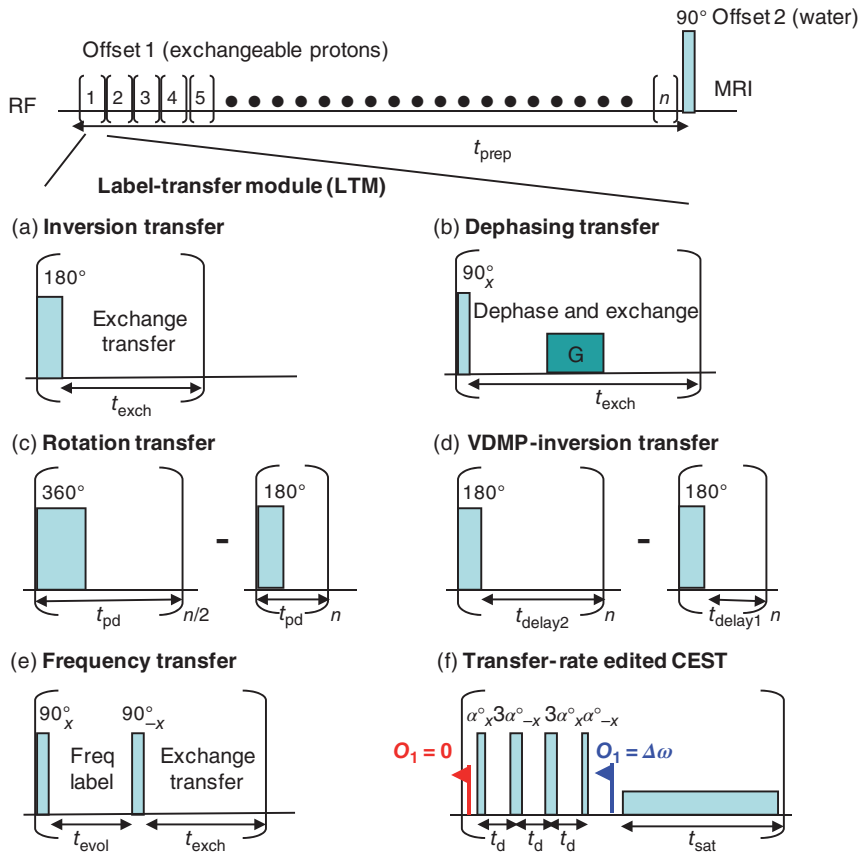

Figure 10. Exchange transfer pulse sequences employing excitation. The preparation time (t_{prep}) consists of a series of label transfer modules (LTMs), during which exchangeable protons are labeled and transferred. This can be achieved using frequency-selective inversion (a), excitation + dephasing (b), or by employing the difference between frequency-selective signals acquired at multiple rotation angles (c) or transfer delays (d), as a way to compensate for interfering saturation effects. Alternatively in (e), a range of frequencies covering multiple proton types are excited and the frequency of the protons modulated using chemical shift evolution during an evolution time (t_{evol}). After this, the magnetization is returned to the longitudinal axis and the frequency modulation is transferred to water. In the LTM for the transfer-rate-edited (TRE-) CEST approach in (f), all spins except for water are rapidly excited using an on-resonance binomial pulse. This is followed by selective saturation of a component at offset $\Delta\omega$. Note that the relative time scales for this module are not displayed proportionately: the nonselective excitation takes about 2 ms total and the selective saturation is ~100 ms

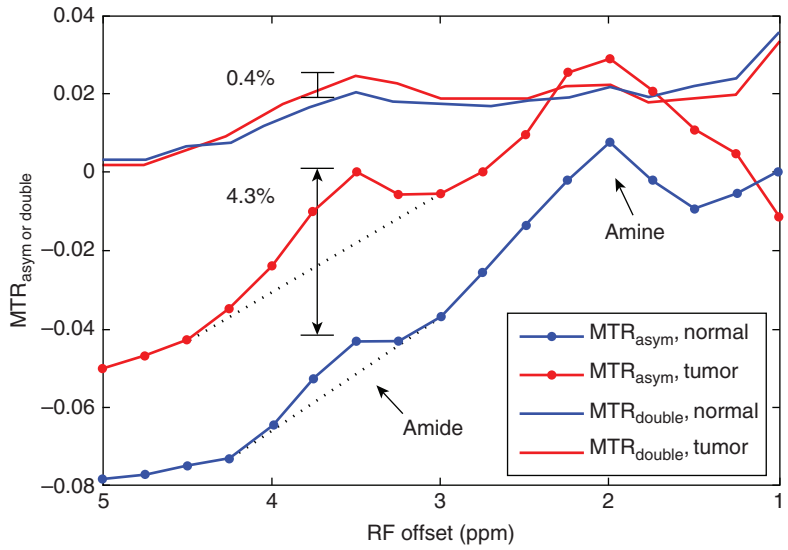

Figure 11. Comparison of CERT and APTw MRI effects for a rat brain with a 9L glioma. Clean APT effects are visible for CERT (MTR_{double}), which are much smaller than the combined effects in conventional CEST (MTR_{asym}), where the APT effect can be seen on top of the broader asymmetric rNOE and MTC contributions. (Reproduced with permission from Ref. 102. © John Wiley & Sons Ltd., 2014)

still contain contamination from other exchangeable protons resonating at these frequencies. They are suitable for dynamic imaging, for instance, when infusing a contrast agent, but need additional editing for endogenous protons.

Rotation Transfer. The rotation transfer experiment is also frequency selective, but exchange-transfer signals sensitive to rotation can be selected out when subtracting signals from sequences containing pulses of different flip angle, but the same average irradiation power,[75] $B_{avg,power} = \sqrt{\frac{1}{\tau_{pd}} \int_0^{\tau_{pd}} B_1^2 dt}$ over the LTM of length τ_{pd}. An example is the chemical exchange rotation transfer ('CERT'; Figure 10c) approach,[101] which uses angles of 360° and 180°. Simulations show that MTC saturation effects and DS are independent of flip angle under such conditions.[101] It is important to realize that the water proton pool, while also having a long T_2, is saturated and not rotated provided that the adiabatic condition is fulfilled, which is the case for flip angles greater than about 50°. The CERT effect is measured using the parameter

$$\begin{aligned} MTR_{double} &= MTR(\Delta\omega, \pi) - MTR(\Delta\omega, 2\pi) \\ &= \frac{S_{sat+rot}(\Delta\omega, 2\pi) - S_{sat+rot}(\Delta\omega, \pi)}{S_0} \\ &= \frac{S_{rot}(\Delta\omega, 2\pi - \pi)}{S_0} \end{aligned} \quad (12)$$

Because the exchangeable protons experience both saturation and rotation and only the effect of rotation remains, there is a substantial B_1-dependent SNR loss (~50% for a typical CERT experiment with a typical average B_1 of ~1.6 μT in vivo). However, this is worthwhile in view of the greatly enhanced selectivity for the protons of interest due to removal of the MTC, DS, and lipid interferences, as well as a much reduced sensitivity to B_0 inhomogeneity. The latter is because small changes in B_0 will not affect the signal difference for a resonance with a width of tens of hertz in a Z-spectrum. Thus data need to be acquired only at a single frequency, which allows for signal averaging to improve overall SNR per unit time, as compared to acquiring an entire Z-spectrum to determine the water offset frequency in a typical CEST experiment.

It is possible to sensitize CERT to slow exchange (to filter out hydroxyl and amines: a so-called 'exchange low-pass filter') when the average B_1 is such that the adiabatic condition applies. This is generally the case at high B_0 but often not at 1.5 and 3 T. An example of clean editing is shown in Figure 11, where the CERT effects (difference of 300 2π-pulses and 600 π pulses with $B_1 = 1.6$ μT and $t_{sat}(\pi) = 6.8$ ms) in a 9L glioma model are compared with conventional APTw MTR_{asym} measures.[102] While showing a clear pure APT increase in tumor for the parameters used, MTR_{double} is much smaller than the APTw MRI increase based on asymmetry analysis. This arises because the APTw MRI is contaminated with asymmetric contributions due to rNOEs and MTC. Therefore, a clinical APTw MRI may be more practical because all of the effects are cumulative for detecting tumor presence (see section titled 'Amide Proton Transfer Weighted (APTw) MRI').

VDMP Inversion. The VDMP approach explained in the previous section can also be performed using frequency-selective inversion pulses to maximize the effect (Figure 10d). This approach can be employed with a high B_1 and a limited number of pulses (16–64, $B_1 = 3.4$ μT, $t_{sat} = 20$ ms) to provide a sufficient CEST effect.[69,73] The RF pulses serve both as a relaxation filter for the interfering saturation contributions as well as an exchange rate filter for the CEST contributions. This enables application to many different types of protons.

Frequency Transfer. Inversion transfer, dephasing transfer, and rotation transfer require the use of frequency-selective pulses, which is inconvenient when the goal is to simultaneously edit multiple types of protons. A pulse sequence that allows for the

simultaneous excitation and editing or removal of different components despite all being part of a single water-signal reduction is the frequency-labeled exchange transfer (FLEX, Figure 10d) method.[100,103] The frequency encoding occurs during evolution periods, (t_{evol}), during which chemical shift (frequency offset)-dependent evolution of the transverse magnetization of the exchangeable solute protons occurs. This magnetic labeling leads to t_{evol}-dependent amplitude modulation of the bulk water signal based on frequency information that is specific to the individual CEST agent protons.

While the signal attenuation of multiple contributing proton types is convolved within the amplitude modulation of the single bulk water signal, this information can be subsequently reconstructed into the original frequency components using FT NMR methods known from high-resolution NMR, but now with water sensitivity. An additional advantage of this approach is that short-T_2 components, such as the MTC, are not frequency labeled and disappear quickly at short t_{evol}. They can thus be filtered out by removing the first time-domain points (in the microsecond range) or by separating out the components via time-domain analysis of the acquired signal. This procedure is illustrated in Figure 12 for infusion of a paraCEST agent[104,105] in vivo. Simple FT of the data gives a complicated spectrum with several components that can be resolved by time-domain fitting.

Transfer-rate Edited CEST. Recently, a hybrid excitation–saturation sequence was proposed that can be used to edit out slowly transferring components, while retaining the fast-exchanging proton signal.[106] The LTM of this transfer rate-edited CEST (TRE-CEST) approach (Figure 10f) contains a non-selective binomial pulse applied at the water frequency. The binomial pulse rapidly excites a large part of the frequency spectrum but with a band-pass filter on water, similar to the on-resonance MTC approach in Figure 6(b2). This rapidly labels all exchangeable protons with excitation, and is followed by a frequency-specific saturation, which further labels a specific proton. If a proton exchanges rapidly, the saturation pulse will keep labeling it, and the label is continuously transferred to the water signal. Meanwhile, slow-exchanging protons are already labeled and cannot be saturated further since the saturated proton is not yet exchanged. They will thus not contribute additional labeling to the water. This approach was able to successfully separate out the slow rNOE contribution in egg white and bovine serum albumin samples, removing a large fraction of the rNOE signal while retaining the amide proton signals.[106]

The development of excitation- and delay-time based approaches for CEST agents is actively ongoing. For instance, on-resonance versions of the FLEX and VDMP approaches have been reported,[107,108] which extend the opportunities for spin editing, especially for fast-exchanging protons that are

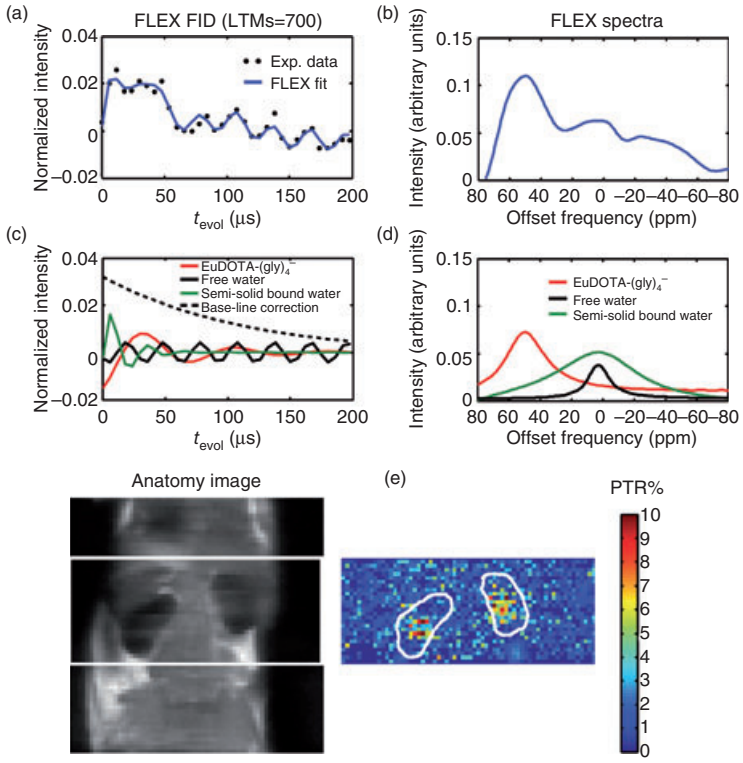

Figure 12. In vivo FLEX-MRI of mouse kidneys after an injection of the paraCEST agent (EuDOTA(gly)$_4$ at 0.25 mmol kg^{-1}) via the tail vein. (a) FLEX signal decay (700 LTMs) within a region of the left kidney; (b) FLEX spectrum generated by FT of (a) shows the paraCEST peak at 50 ppm convolved with a broad MTC profile. (c) Details of time-domain analysis and (d) spectral components of the FLEX signal showing paraCEST agent bound water (red line), free water (black line) and semisolid bound water (green line). The black dashed line shows the baseline correction. (e) Pixel-by-pixel in vivo paraCEST map shows a high PTR level from the paraCEST agent within the kidneys. (Reproduced with permission from Ref. 105. © John Wiley & Sons Ltd., 2014)

efficiently and repetitively labeled. They are similar to the TRE-CEST approach, but do not require a long saturation pulse in the LTM. As such, the above overview is not inclusive and is meant only as a brief introduction to the principles.

Data Analysis for CEST Spectra

As we have seen, the in vivo CEST spectrum is complex. In addition to the symmetric DS and the asymmetric MTC contributions originating from semisolid tissue components there are substantial contributions from multiple endogenous metabolites and tissue building blocks with exchangeable amide, amine, imino, or hydroxyl protons, or relayed NOEs from aliphatic protons in mobile MMs. Figure 5 shows some of these effects in a study of the knee in which gags were detected. When increasing the RF power, the ratio of the different signal contributions changes. Slower exchanging species dominate at low B_1 and faster ones dominate at high B_1 because the saturation efficiency depends on the exchange rate [equation (7)]. In addition, the DS line broadens and the MTC effect increases strongly. Such interference is not a major issue when using exogenous contrast agents, as these can be studied using time-dependent signal differences in dynamic scanning. This was demonstrated recently for glucose imaging.[109,110] However, whenever detection of endogenous molecules at equilibrium is the goal, care is warranted as it is difficult to cleanly separate out individual proton moieties from the broad overlapping components that often arise in the saturation spectrum. Indeed, the majority of papers in the literature, including those about detecting Glu, Cr, sugars (e.g., glucose, Mi and glycogen), urea, or amide protons in proteins and peptides, employ MTR_{asym} analysis, which includes aliphatic signal contributions [see equation (9)]. The editing sequences in the section titled 'Pulse Sequences for MTC and CEST MRI' are a first step toward approaches that either do not require asymmetry analysis or remove components that interfere. In the following two sections, we briefly discuss how to address some of the issues that complicate asymmetry analysis and some alternative data-fitting approaches for Z-spectra.

MTR_{asym} Analysis

MTR_{asym} analysis of the Z-spectrum (Figure 4c and d) is useful in vitro to remove DS effects but fails for metabolite-specific proton detection in vivo because of the contamination by aliphatic components [see equation (9)] and overlapping exchangeable protons from other compounds. An additional common problem with this approach is interference from aliased fat signals. Fat artifacts are especially cumbersome in APTw MRI because the chemical shift difference between lipid and water is the same as that between amides and water (i.e., 3.5 ppm for amides and −3.5 ppm for lipids). Lipid ghosts are common when using fast imaging methods such as echo planar imaging (EPI). Fat suppression can be added to the pulse sequence either by using a frequency selective refocusing pulse[111] or, if the fat is spatially separated, by outer volume suppression approaches, such as those used in 3-D APTw GRASE imaging.[50]

Spatial inhomogeneity in B_0 leads to different voxels in the image experiencing a shift from the spectral minimum with respect to the spatially averaged bulk water reference frequency. Asymmetry analysis is extremely sensitive to such shifts because the spectral intensity change is very steep around the minimum, leading to inaccuracies that may be bigger than the actual CEST effects of interest. The simplest approach for correction is to determine the voxel water frequency from the actual Z-spectrum by spline or high-order polynomial fitting, with the assumption that this frequency is the lowest signal intensity. This is followed by centering of the spectra for each voxel. Acquisition of Z-spectra is time consuming and the SNR of CEST spectra is often low. In order to increase the SNR, Zhou *et al.*[112] measured CEST data, by repeating acquisitions at just three spectral points around the frequency of the CEST target at $\pm\Delta\omega_s$. However, this approach is not accurate when any CEST contrast overlaps with the water frequency causing the minimum to broaden asymmetrically. This typically happens with hydroxyl groups in sugars at lower B_0 field or at high B_1. When a three-point Z-spectral fit is not possible, actual B_0 mapping is required, followed by spectral shifting for each voxel. An algorithm suggested by Sun *et al.* corrects three-point CEST scans for B_0 inhomogeneity using a gradient-echo based B_0 map.[113]

The most accurate method for B_0 correction is the WAter Saturation Shift Referencing (WASSR) approach, in which a pure DS image is obtained using on-resonance saturation pulses whose power and duration are sufficiently low such that the interfering effects of MTC and CEST are avoided.[114] This method, which was shown to have an accuracy of ≤1 Hz, is particularly beneficial for corrections of B_0 in cases with small chemical shift differences between the water protons and the exchanging protons, such as in the case of sugars, e.g., glycogen[114–116] and D-glucose.[24,116–118] The voxel shifts can be recovered from the WASSR data either by Z-spectral asymmetry analysis[114] or by Lorentzian fitting of the clean saturation spectrum.[119] A question that is often asked is how the WASSR information differs from that in a typical gradient-echo B_0 map that could be acquired faster. The answer is twofold. Most importantly, while a standard field map provides correct voxel shift differences with respect to the bulk water frequency, the center frequency of this bulk water signal in the reference voxel may be offset. Consequently, the exact center frequency for a particular voxel is unknown within a few hertz, which is the precision needed for these CEST experiments. Secondly, the WASSR image acquisition protocol is identical to that in CEST. Therefore, the B_0 field is not susceptible to spatial distortions and eddy currents that may affect field maps acquired with different imaging parameters, such as with gradient-echo imaging.

Analysis of CEST Spectra without Asymmetry Analysis

When studying protons in the slow-exchange regime ($k_{sw} \ll \Delta\omega_{sw}$), resonances of the solute protons are separated sufficiently from the water ^{1}H resonance to allow fitting of the latter if it has a well-defined shape. The saturation lineshape is pure Lorentzian for protons in liquids and such fitting can be achieved if MTC contributions are small, which is the

case in phantoms or at a low saturating RF power in vivo. In such cases, the DS contribution can be removed in large part by using a Lorentzian fit of the water line:

$$(A, b.\mathrm{LW}_{1/2}, f_{\mathrm{shift}}) = 100 - A\left(\frac{(\mathrm{LW}_{1/2})^2}{(\mathrm{LW}_{1/2})^2 + 4(f_0 - f_{\mathrm{shift}})^2}\right) + b \quad (13)$$

where A is the amplitude, $\mathrm{LW}_{1/2}$ is the linewidth of water at half maxima, f_{shift} is the frequency shift of the minima, and b is the baseline offset to be fitted from the experimental data at the center of the water peak. This correction is used first to quantify and adjust for the signal frequency-drift in each voxel and subsequently to remove the DS contribution using a LD analysis. The transferred saturation is the difference between the fitted water Lorentzian and the Z-spectrum:

$$\mathrm{LD}(\Delta\omega) = \frac{S_{\mathrm{sat}}^{\mathrm{DS}}(\Delta\omega)}{S_0} - \frac{S_{\mathrm{sat}}(\Delta\omega)}{S_0} = \mathrm{MTR}(\Delta\omega) \quad (14)$$

This method was demonstrated by Liu *et al.*[119] for some paraCEST agents in phantoms and by Jones *et al.*[71,72] in vivo in the human brain (Figure 7b and d). In Figure 13, the upfield LD spectrum of the right posterior lobe in human brain is compared with ^{1}H MRS data from the same region. After processing the MRS data into mobile MM and metabolite contributions, the MM data were compared with the LD. While agreement is evident for a number of resonances, it was later concluded that a broader component from residual MTC was still present in the LD data, causing enhancement of WM in LD-based images.[71,72] Around the same time, Zaiss *et al.*[120] theoretically demonstrated the possibility of estimating and removing DS and MTC contributions with Lorentzian fitting when the weak-saturation pulse condition is applicable. In a related approach, CEST effects have also been filtered from other MTC and DS effects by using time-domain analysis in an approach known as *time-domain removal of irrelevant magnetization* (*TRIM*).[121] Here, the frequency domain data is converted into the time domain by inverse FT and any lineshape can be used to fit the data. These data are then normalized by the dwell time, after which the fitted data without DS and MTC is again converted back to the frequency domain by FT and the residual Z-spectra analyzed for CEST and rNOE effects.

A very simple approach for analyzing single CEST contributions is to approximate the broad background signal with some type of fitting (generally an extrapolated least-squares fit of the baseline over the frequency range of interest) and then subtract this baseline to approximate the CEST effect. Again, this is most

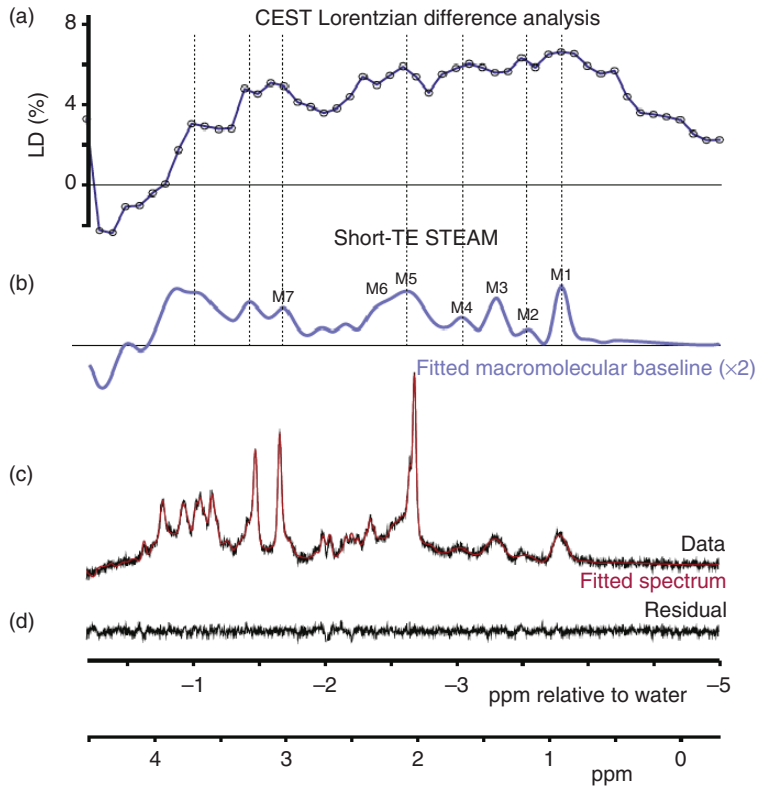

Figure 13. Comparison of the appearance of rNOE-based Lorentzian difference data from a region in the right posterior portion of the brain (a), with ^{1}H MRS data (b–d) from the same approximate area. The ^{1}H spectrum was fit for metabolites (c), several mobile MM components, and a baseline (d). The MM components and baseline were combined to create a fitted MM baseline spectrum (b). Peaks (M1–M7) in this spectrum were assigned according to Behar *et al.* [46] Dashed lines correlate the peaks in the fitted MM baseline (b) with the NOE LD data in (a). The upper scale has water centered at 0 ppm, while the lower traditional ^{1}H MRS scale has NAA set to 2.02 ppm. (Reprinted from Neuroimage, 77, C. K. Jones, A. Huang, J. Xu, R. A. Edden, M. Schar, J. Hua, N. Oskolkov, D. Zaca, J. Zhou, M. T. McMahon, J. J. Pillai and P. C. van Zijl, Nuclear Overhauser enhancement (NOE) imaging in the human brain at 7 T, 114. © 2013, with permission from Elsevier)

useful for spectra in the slow-exchange regime, which applies mostly to low-B_1 data acquired in vivo.[122] However, it has also been used for analysis of well-shifted resonances of hydrogen-bonded protons.[123]

Another potentially useful data analysis approach is the so-called normalized magnetization transfer ratio (NOMAR) approach. NOMAR spatially segments out tissue components with low MTC effects by using signal-intensity ratios from Z-spectral points acquired at two offsets outside the ^{1}H spectral range (12.5 and −50 ppm) that are only sensitive to MTC contrast. This has been shown to remove contamination from cerebrospinal fluid, blood, and edema.[124]

Quantification of CEST-related Parameters

It is no doubt clear from the previous sections that there is a lot of ongoing effort by CEST researchers to analyze the different contributions to the Z-spectrum and edit these in or out[73,120,125–131] to provide more specific measurements of individual spectral components. The reason of course is to quantify endogenous and contrast-agent contributions as well as other parameters in the CEST equations that can provide information regarding physiological processes in vivo. The theoretical description of WEX and CEST data is well established[12,24,57,61,62,66] and analytical equations are available for calculating parameters for moieties undergoing slow exchange on the NMR time-scale [e.g., equations (6)–(8)]. It is especially noteworthy that the presence of a concentration ratio (x_s) of CEST agent protons relative to the water protons allows an intrinsic quantification of metabolite ratios. Furthermore, since the water concentration in the cytosol and extracellular space can be assumed to be 55.5 M (or 111 M protons), absolute molar concentrations in this should be attainable, and such measurements have already been demonstrated in phantoms. For this purpose, it is of course necessary to determine the other parameters in equations (6)–(8). Note that such a concentration determination requires knowledge only of R_{1w}, in contrast to water-referenced MRS, where knowledge of R_1 and R_2 of both water and the protons of interest is required. To obtain tissue concentrations (in mole per milliliter tissue volume or gram weight), a tissue water content correction will be needed, which is known for many tissues.

Several methods have been suggested for measuring exchange rates, which is possible through their dependence on the saturation power and time.[98,132] For slowly exchanging species such as the amide protons, exchange rates have been estimated using WEX spectra.[43,62] FLEX data have also been shown to allow quantification of concentrations and exchange rates.[100,104] Importantly, the analytical CEST equations (6)–(8) apply only for sufficiently slow exchange on the MR time-scale and Bloch equation fitting has to be used for rates that fall outside this regime. When quantifying effects, it is important to keep in mind that the quantification depends on knowledge of B_1, and that accuracy may be impaired by B_1 inhomogeneity. To correct for B_1 inhomogeneity, it is useful to measure B_1 maps,[133] from which Z-values for different B_1 values can be interpolated for each pixel, and an MTR_{asym} map generated. In a related method, referred to as the 'n-point Z-B_1 correction' and the 'n-point contrast B_1 correction',[134] the MTR_{asym} calculation is performed after a Lorentzian fit is applied prior to the interpolation of contrast for every B_1. Inhomogeneity in B_1 is typically not an issue in clinical scanners at 1.5 T and is a relatively minor problem with dual-channel transmit instruments at 3 T. It is an issue at 7 T, but that should ameliorate with new eight-channel transmit hardware becoming available.

Potential and Clinical Translation of CEST Methods

The potential and significance of CEST MRI are reflected by the rapidity with which the field is expanding and being adopted. As of this writing, the original paper by Ward and Balaban and coworkers[7] has been cited 617 times (Google Scholar, January 2016) and about 70–80 times per year in the past 5 years. Three recent dedicated CEST workshops (3rd, 4th, and 5th international CEST workshops in Annapolis, 2012, Torino, 2014, and Philadelphia 2016) drew about 90–200 registrants. The last decade has shown major developments for paraCEST agents,[14,15,20,89,90,119,135–148] diaCEST agents,[12,13,17,42,43,68,72,88,102,116,125,128,149–160] and even hyperpolarized (hyperCEST) agents.[161,162] This is not surprising in view of the number of potential applications including pH imaging, metabolite detection, ion detection, cellular protein and peptide imaging, cell labeling, temperature imaging, detection of enzyme activity, CEST reporter genes, and the imaging of sugars. Another important development is the use of CEST agents in liposomes (lipoCEST)[142,143] to detect picomolar concentrations of these nanoparticles via the exchange of water between intra- and extraliposomal environments.[16,142,143,163,164] While the paraCEST, lipoCEST, and hyperCEST agents show much potential, due to space limitations this remaining section will focus on some of the diaCEST applications that have actually been applied in humans.

Amide Proton Transfer-weighted (APTw) MRI

Based on phantom studies on proteins[12] and WEX data in cells,[1,6] it was hypothesized that it should be possible to detect the amide protons of mobile proteins and peptides in tissue via the water signal. This APT process was demonstrated in vivo in 2003.[42,43] In the APT method, the composite amide resonance at around 8.25 ppm in the ^{1}H spectrum is detected at about 3.5 ppm in the Z-spectrum relative to water (Figure 3c and d). Subsequently, APT was used to detect pH changes during early ischemia (based on the pH dependence of the amide proton exchange rate)[43,62,88] and increases in the mobile protein/peptide content of brain tumor tissue.[42,165] In these studies, CEST effects were assessed using MTR_{asym} analysis and, due to contamination by other transfer processes,[21,42,43,53,72,102,125–128,130,131,166] it is most appropriate to refer to the contrast achieved as APTw. In studies of cancer in the brain, APTw MRI is showing promise for (i) separating high-grade tumors from low-grade tumors and edema;[42,112,167] (ii) distinguishing recurrent tumor from treatment necrosis;[159] and (iii) detecting early response to treatment.[159,168] In addition, APTw MRI allows differentiation of acute ischemia

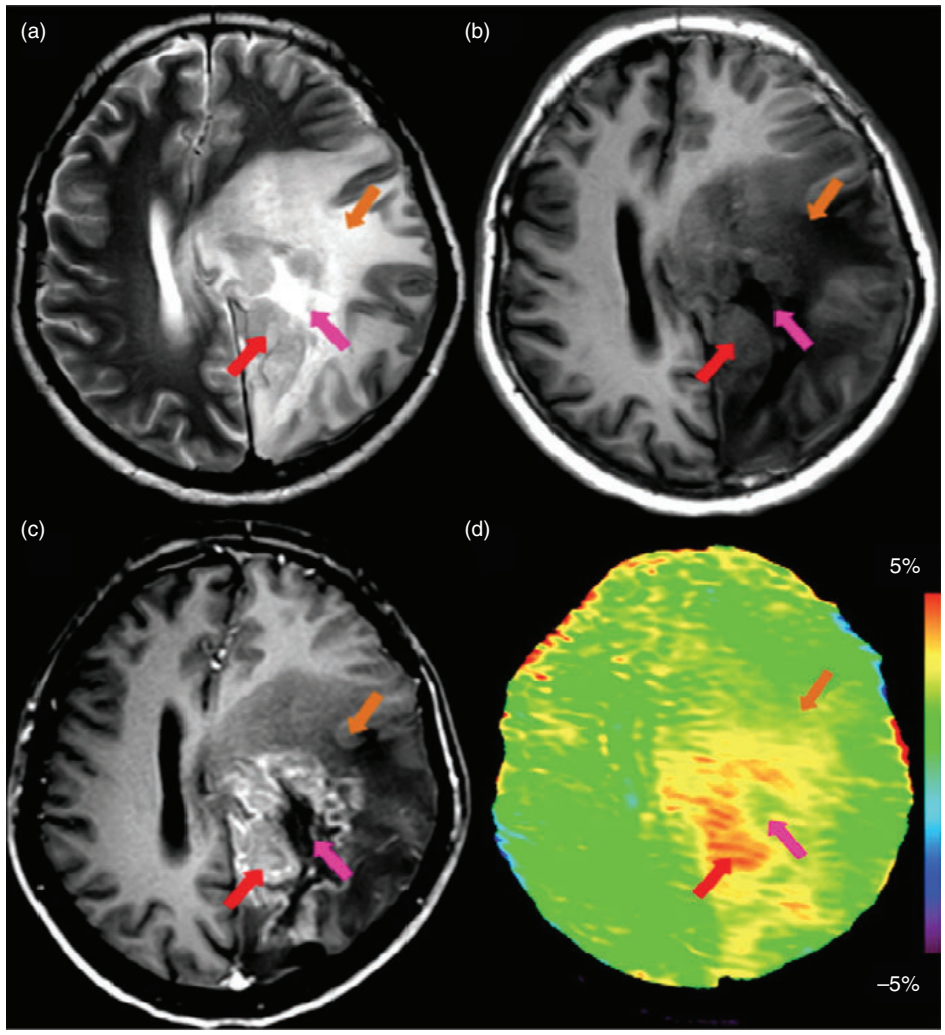

Figure 14. MRI in a patient with recurrent astrocytoma (grade III), acquired 4 months after treatment. (a) T_2-weighted image shows the recurrence of glioma with heterogeneous hyperintensity in the left parietal lobe; (b) T_1-weighted image shows a heterogeneously hypointense lesion. The exact location of the tumor core is unclear. (c) Post-contrast T_1-weighted image reveals a gadolinium-enhancing tumor core (red arrow) and a necrotic area (pink arrow). The recurrent tumor is associated with the surrounding edema and mass effect. (d) APT image showing a clear increase in APT signal intensity in the tumor core, identified by the gadolinium-enhanced T1-weighted image. The regions of necrosis (pink arrow) and edema (orange arrow) are almost isointense on APT. (Reprinted from Neuroimage, 51, Z. Wen, S. Hu, F. Huang, X. Wang, L. Guo, X. Quan, S. Wang and J. Zhou, MR imaging of high-grade brain tumors using endogenous protein and peptide-based contrast, 616. © 2010, with permission from Elsevier)

from hemorrhage.[169] APTw MRI has been implemented on clinical scanners[50,112,153] and is being evaluated clinically at several institutes for assessing brain tumors,[112,167,170–173] breast tumors,[17,174] prostate cancer,[175] head and neck cancer,[176] and ischemic stroke.[177] Figure 14 shows an example of APTw data from a patient with a recurrent astrocytoma.

Glycosaminoglycan CEST (gagCEST)

Gag is a main constituent of cartilaginous tissues whose concentration can be used as a potential indicator of the onset of osteoarthritis and intervertebral disc degeneration prior to their morphological manifestation. GagCEST MRI[68] deals primarily with the detection of the exchange effect of three hydroxyl protons of gag (Figure 5a), resonating around 0.9–1.9 ppm downfield of water[68]. The gag molecule also contains an amide proton at 3.2 ppm downfield of water, but its CEST effect is much smaller, because of the difference in exchange rate and availability of one amide proton vs. the three hydroxyl protons. Experiments at 3 and 7 T have shown a correlation of gagCEST with sodium (^{23}Na) MRI,[178,179] but not necessarily with ^{1}H MRI T_2 maps.[180] The effect is not easy to detect because of the close proximity to the water resonance, possibly leading to erroneous direct saturation contributions if the water offset is not precise in each voxel. There have been reports that correcting for B_0 inhomogeneities leads to a small to negligible gagCEST signal at 3 T in the healthy knee (about 2%). That problem has been countered by going to higher B_0 (e.g., 7 T), where a 6% gagCEST effect could be observed together with a high correlation of the results with the standard ^{23}Na imaging technique.[179,181]

GagCEST has also been applied to study nondegenerative lumbar intervertebral discs[182] and may differentiate between the nucleus pulyposus (NP) and annulus fibrosus (AF) of these discs.[183–186] GagCEST technology, similar to the APTw approach, is based on MTR_{asym} analysis and optimization of the process, especially with respect to the correction of B_0 and B_1 inhomogeneities and removal of interference by NOEs, is still ongoing. Applications to larger study cohorts are needed to convert this into a clinically viable technique.

CEST Studies of Glutamate (gluCEST)

Glutamate (Glu) is an excitatory neurotransmitter in the central nervous system (CNS), controlling several signaling processes together with GABA. Cai *et al.*[149] used CEST to study the pH and concentration dependence of the amine protons of Glu resonating at ~3.0 ppm downfield from water and exchanging at a rate of about 5500 s^{-1}. They showed that signals proportional to the Glu concentration could be detected in the human brain. A substantial difference between the Glu concentration in gray and WM was observed, consistent with expectations from positron emission tomography (PET) studies. One issue when looking at Glu via CEST is the presence of some contributions from amide protons, as their average chemical shifts are only about 0.5 ppm apart at 3 T. Another issue is the use of MTR_{asym} analysis. However, it was demonstrated that the majority of the signal was due to Glu by using a saturation pulse train of high B_1 and shorter duration than the low-power, long-duration saturation pulses needed for optimal APTw MRI.[187] Such gluCEST experiments have since been performed on the healthy human brain and spinal cord, and in studies of the preclinical onset of Alzheimer's.[188–190] In a recent study on patients with temporal lobe epilepsy, Davis *et al.*[191] showed that gluCEST could correctly lateralize a seizure focus in temporal lobe epilepsy, whereas assessment by conventional MRI could not show a hemispheric difference.

CEST Studies of Creatine (CrCEST) and Glycogen (glycoCEST)

Creatine (Cr) and phosphorylated creatine (phosphocreatine, PCr) play a role in phosphate-bond energy storage and transmission, and are found in many organs, including the brain, heart, and skeletal muscle. The guanidine protons from the two creatines resonate at 1.8 ppm from water and can be detected by CEST MRI.[192] Creatine CEST (CrCEST) has been applied for temporal mapping of muscle energetics post-mild exercise in humans.[154,193] CrCEST provides an alternative to ^{31}P MRS studies of PCr, which participates along with the unphosphorylated component Cr in the creatine kinase reaction. CrCEST offers a potentially greatly enhanced sensitivity due to the combined effects of the larger gyromagnetic ratio of ^{1}H and, most importantly, the very large CEST enhancement due to the relatively fast exchange rate of Cr ($k_{sw} \sim 950$ Hz) in the physiological pH range. With a favorable choice of saturation parameters ($B_1 \sim 4\,\mu T$), Cr could be resolved from PCr ($k_{sw} \sim 120$ Hz) and ATP (adenosine triphosphate; $k_{sw} \sim 120$ Hz), and showed a sensitivity about 1500 times higher than ^{1}H MRS of Cr at 3 T.[192] Reddy *et al.* have published several studies applying CrCEST to measure active muscle metabolism in the leg[154,193] and the heart.[152]

While these studies show great potential, it must again be remembered that they are in part based on MTR_{asym} analysis. To study differences during exercise one could simply perform dynamic studies of effect differences at one frequency, but there may still be interference from other CEST-sensitive compounds that resonate nearby. For instance, glycogen hydroxyl groups resonating at 1.2 ppm have a large CEST effect called glycoCEST[115,116] that will also be affected by saturation at 1.8 ppm because of the broad lineshape (fast exchange rate). Based on the type of exercise, the glycogen may have an opposite effect as it depletes while unphosphorylated Cr increases. In addition, the OH groups of carbohydrates such as glycogen and glucose will affect the T_2 of water,[194,195] which also affects the saturation lineshape. The glycogen hydroxyl moiety also broadens the water line asymmetrically so that use of an accurate B_0 reference method to determine the Z-spectral minimum is essential.[114] On the other hand, the Cr level is low in the liver, and glycoCEST may be more useful, and is indeed being tried in humans.[196,197] However, glucose signals will overlap with those of glycogen and, when using MTR_{asym}, NOE effects may also be mixed in. Thus, further editing will likely be needed to cleanly separate out these effects in the leg and the liver.

FDA-approved Agents that are Suitable for diaCEST Studies

Contrast agents are important to provide increased specificity and sensitivity for visualizing anatomy and physiology in ways that are not attainable with standard, noncontrast imaging capabilities. The field of molecular MRI encompasses the design of tissue-specific, pathology-specific and/or physiology-specific smart probes. However, a recent NIH meeting (2014) that evaluated the status of molecular imaging showed a disappointing lack of new MRI probes being translated to the clinic in recent years.[198] The main problem is that all of the MRI agents currently used clinically and most of the smart agents proposed for molecular MRI, contain paramagnetic or ferromagnetic metals to induce changes in the relaxation times T_1 or T_2. While they are extremely safe overall, there are reports of toxicity of some metallic MRI contrast agents in some patients with kidney disease. Consequently, such agents are under increased scrutiny by the US Food and Drug Administration (FDA), complicating the approval process and delaying the availability of newly designed agents that could benefit patients. Thus, there is a need to simplify, expedite and de-risk the approval process by developing MRI agents with proven low toxicity and/or with agents previously demonstrated to be suitable for clinical use based on other indications. CEST MRI allows us to break this barrier by opening up a new range of possible agents.

Imaging agents that are already approved for other modalities constitute a first class of compounds with the potential for fast translation into clinical MRI. For example, it was recently demonstrated[199–204] that the CT agents iopamidol and iopromide, which contain multiple amide protons, can

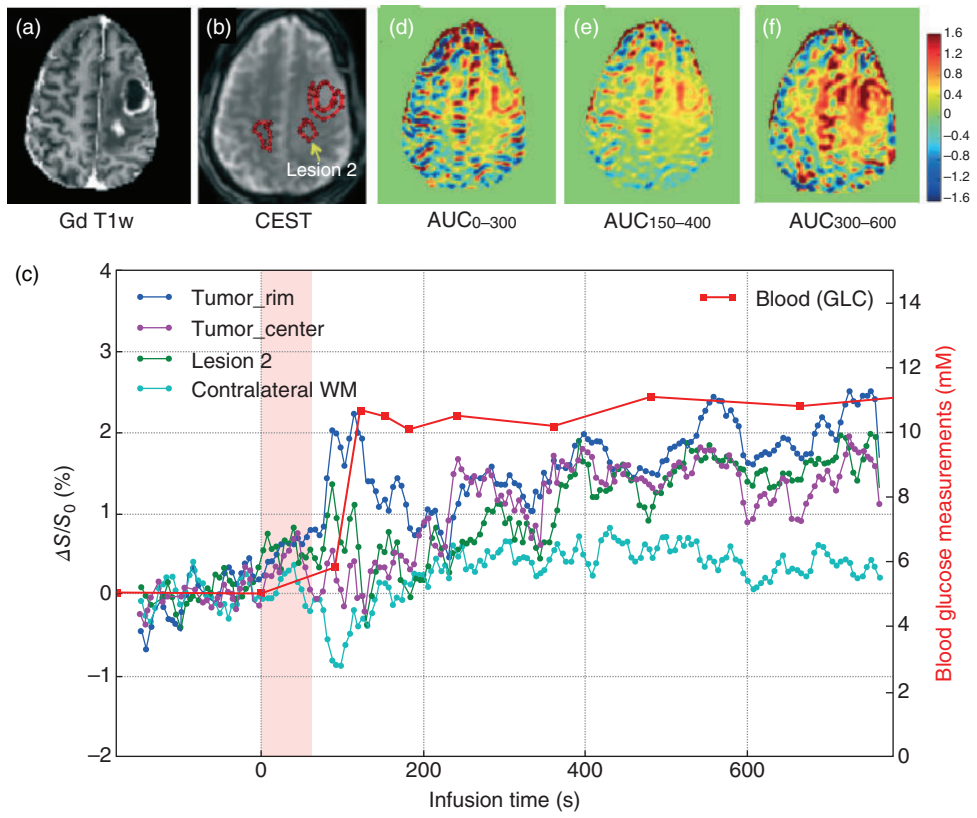

Figure 15. Results from a dynamic glucose enhanced (DGE) MRI study of a patient with an anaplastic astrocytoma. At top, T_2-weighted (a) and Gd T_1-weighted (b) images and DGE-based area under the curve (AUC) images (d–f) for different time periods relative to the start of infusion. The dynamic time curves for several regions of interest are shown in (c), as compared to the glucose level measured in a vein contralateral to the infusion arm (red, scale at right). (Reproduced from Ref. 110. © Tomography, 2015)

be used for in situ pH assessment using CEST. A second class of agents with high translation potential consists of natural compounds, such as sugars, peptides, and proteins, that are approved for other indications. Actually, D-glucose is already approved by the FDA for the intravenous glucose-tolerance test[205] for patients with diabetes, allowing its fast translation to CEST MRI studies in humans. Recently, two groups[117,118] contemporaneously demonstrated in animals the potential use of D-glucose as a contrast agent for cancer detection. This has been followed by several other papers on glucose and glucose analogs.[206,207] Dynamic glucose enhanced (DGE) imaging has been demonstrated on a glioma mouse model,[109] and recently, the first human data were published.[110] Figure 15 shows some of the preliminary data from a cancer patient.

Conclusions

The field of CEST imaging has been around for 15 years. After a slow start with only a few groups performing such studies it has recently burgeoned. New technologies for editing CEST agents are frequently published and many options for such methods have yet to be explored. The possibilities for novel agent design and for the imaging of mM-level endogenous compounds with water sensitivity is expected to make this relatively new field grow even faster in the future.

Acknowledgments

We are grateful to Dr. Nirbhay Yadav and Dr. Jiadi Xu for carefully reading this manuscript. In addition, we acknowledge the NIH funding for our CEST research from NIH throughout the past decade via grants from NIBIB: RO1 EB015032, RO1 EB015031, RO1 EB009731, P41 EB015909, R01 EB019934, RO1 EB002634, P41 RR15241, RO1 NS083435; P50 CA103175, and R01CA166171.

List of Abbreviations

APT	amide proton transfer
CERT	chemical exchange rotation transfer
CEST	chemical exchange saturation transfer
CHESS	chemical shift selective
CNR	contrast-to-noise ratio
Cho	choline
Cr	total creatine (phosphorylated + unphosphorylated)
DRYSTEAM	Dry Stimulated Echo Acquisition Mode
DS	direct water saturation
FISP	fast imaging with steady precision
FLEX	Frequency Labeled Exchange
GABA	gamma-amino butyric acid

gag	GlycosAminoGlycan
Gln	glutamine
Glu	glutamate
GM	gray matter
GRASE	Gradient And Spin Echo
LD	Lorentzian difference
LOVARS	Length and Offset Varied Saturation
LTM	label transfer module
LU	Lovars unit
LW	line width
meLOVARS	Multi-Echo Length and Offset Varied Saturation
MI	myoInositol
MM	macroMolecule
MTC	magnetization transfer contrast
MTR	magnetization transfer ratio
NAA	N-acetyl aspartate
NOMAR	Normalized Magnetization Ratio
OPARACHEE	ON-resonance Paramagnetic Chemical Exchange Effect
PTR	proton transfer ratio
RARE	rapid acquisition with relaxation enhancement
SAFARI	Saturation with Frequency Alternating RF Irradiation
TI	inversion time
TRE-CEST	Transfer-Edited Chemical Exchange Saturation Transfer
TRIM	time domain removal of irrelevant magnetization
VDMP	variable delay multi pulse
WASSR	Water Saturation Shift Referencing
WATERGATE	WATER suppression by Gradient Tailored Excitation
WEX	Water Exchange spectroscopy
WM	white matter
ZAPI	Z-spectroscopy with Alternative Phase Irradiation

Biographical Sketches

Peter C.M. van Zijl MS, 1980, Chemistry. PhD, 1985, Mathematics and Physics (Physical Chemistry), Free University, Amsterdam, The Netherlands. Fellow, 1985–1987, Chemistry, Carnegie Mellon University; Fellow, 1987–1990, National Cancer Institute, NIH; Assistant Professor of Pharmacology, 1990–1992, Georgetown University; Johns Hopkins University, Department of Radiology, Associate Professor 1992–1997; Professor 1997 to present. Founding Director, F.M. Kirby Research Center for Functional Brain imaging 1999 to present. Fellow ISMRM, 2004. Gold medal, ISMRM, 2007 for contributions in MR spectroscopy, diffusion imaging, and functional MRI. Distinguished Investigator, Academy of Radiology Research, 2012. Laukien award, 2016 for contributions to CEST MRI. Current research interests: physiological and functional MRI, exchange and magnetization transfer MRI and spectroscopy, development of non-metallic biodegradable contrast agents, protein and carbohydrate MRI, susceptibility tensor MRI.

Akansha Ashvani Sehgal MSc 2011, Physics, Indian Institute of Technology Roorkee, India. PhD (Physical Chemistry) 2014, University of Pierre and Marie Curie, Paris, France. Post-doc fellow 2014–2015, Ecole Normale Superieure, Paris, France. Post-doc fellow, 2015 to present, Johns Hopkins School of Medicine, Baltimore, USA. Current research interest is methodology development of exchange and magnetization transfer in MRI.

References

1. S. Mori, S. M. Eleff, U. Pilatus, N. Mori, and P. C. van Zijl, *Magn. Reson. Med.*, 1998, **40**, 36.
2. C. Arus, M. Barany, W. M. Westler, and J. L. Markley, *FEBS Lett.*, 1984, **165**, 231.
3. E. L. MacMillan, C. Boesch, and R. Kreis, *Magn. Reson. Med.*, 2013, **70**, 916.
4. E. L. MacMillan, C. S. Bolliger, C. Boesch, and R. Kreis, *Magn. Reson. Med.*, 2016, **75**, 1764.
5. E. L. MacMillan, D. G. Chong, W. Dreher, A. Henning, C. Boesch, and R. Kreis, *Magn. Reson. Med.*, 2011, **65**, 1239.
6. P. C. van Zijl, J. Zhou, N. Mori, J. F. Payen, D. Wilson, and S. Mori, *Magn. Reson. Med.*, 2003, **49**, 440.
7. K. M. Ward, A. H. Aletras, and R. S. Balaban, *J. Magn. Reson.*, 2000, **143**, 79.
8. K. M. Ward and R. S. Balaban, *Magn. Reson. Med.*, 2000, **44**, 799.
9. S. D. Wolff and R. S. Balaban, *J. Magn. Reson.*, 1990, **86**, 164.
10. S. Forsen and R. A. Hoffman, *J. Chem. Phys.*, 1963, **39**, 2892.
11. S. Aime, A. Barge, D. Delli Castelli, F. Fedeli, A. Mortillaro, F. U. Nielsen, and E. Terreno, *Magn. Reson. Med.*, 2002, **47**, 639.
12. N. Goffeney, J. W. Bulte, J. Duyn, L. H.Bryant Jr, and P. C. van Zijl, *J. Am. Chem. Soc.*, 2001, **123**, 8628.
13. K. Snoussi, J. W. Bulte, M. Gueron, and P. C. van Zijl, *Magn. Reson. Med.*, 2003, **49**, 998.
14. S. Zhang, P. Winter, K. Wu, and A. D. Sherry, *J. Am. Chem. Soc.*, 2001, **123**, 1517.
15. S. Aime, D. D. Castelli, S. G. Crich, E. Gianolio, and E. Terreno, *Acc. Chem. Res.*, 2009, **42**, 822.
16. K. W. Chan, J. W. Bulte, and M. T. McMahon, *Wiley Interdiscip. Rev. Nanomed. Nanobiotechnol.*, 2014, **6**, 111.
17. A. N. Dula, S. A. Smith, and J. C. Gore, *J. Neuroimaging*, 2013, **23**, 526.
18. F. Kogan, H. Hariharan, and R. Reddy, *Curr. Radiol. Rep.*, 2013, **1**, 102.
19. G. Liu, X. Song, K. W. Chan, and M. T. McMahon, *NMR Biomed.*, 2013, **26**, 810.
20. A. D. Sherry and M. Woods, *Annu. Rev. Biomed. Eng.*, 2008, **10**, 391.
21. P. C. van Zijl and N. N. Yadav, *Magn. Reson. Med.*, 2011, **65**, 927.
22. E. Vinogradov, A. D. Sherry, and R. E. Lenkinski, *J. Magn. Reson.*, 2013, **229**, 155.
23. M. Zaiss and P. Bachert, *Phys. Med. Biol.*, 2013, **58**, R221.
24. J. Zhou and P. van Zijl, *Progr. Nucl. Magn. Reson. Spectrosc.*, 2006, **48**, 109.
25. M. Piotto, V. Saudek, and V. Sklenar, *J. Biomol. NMR*, 1992, **2**, 661.
26. C. T. W. Moonen and P. C. M. van Zijl, *J. Magn. Reson.*, 1990, **88**, 28.
27. S. W. Englander and N. R. Kallenbach, *Q. Rev. Biophys.*, 1984, **16**, 521.
28. S. Mori, P. C. van Zijl, and D. Shortle, *Proteins*, 1997, **28**, 325.
29. R. A. de Graaf, A. van Kranenburg, and K. Nicolay, *Magn. Reson. Med.*, 1999, **41**, 1136.
30. W. Dreher, D. G. Norris, and D. Leibfritz, *Magn. Reson. Med.*, 1994, **31**, 81.
31. M. J. Kruiskamp, R. A. de Graaf, G. van Vliet, and K. Nicolay, *Magn. Reson. Med.*, 1999, **42**, 665.
32. D. Leibfritz and W. Dreher, *NMR Biomed.*, 2001, **14**, 65.
33. Y. Luo, J. Rydzewski, R. A. de Graaf, R. Gruetter, M. Garwood, and T. Schleich, *Magn. Reson. Med.*, 1999, **41**, 676.

34. S. D. Swanson, *J. Magn. Reson.*, 1998, **135**, 248.
35. S. Mori, C. Abeygunawardana, M. O. Johnson, and P. C. van Zijl, *J. Magn. Reson. B*, 1995, **108**, 94.
36. S. Mori, C. Abeygunawardana, P. C. van Zijl, and J. M. Berg, *J. Magn. Reson. B*, 1996, **110**, 96.
37. R. A. de Graaf, In Vivo NMR Spectroscopy: Principles and Techniques, John Wiley and Sons: West Sussex, England, 2007.
38. W. Dreher and D. Leibfritz, *Magn. Reson. Med.*, 2005, **54**, 190.
39. S. Grzesiek and A. Bax, *J. Am. Chem. Soc.*, 1993, **115**, 12593.
40. S. Mori, M. O'Neil Johnson, J. M. Berg, and P. C. van Zijl, *J. Am. Chem. Soc.*, 1994, **116**, 11982.
41. S. Mori, J. M. Berg, and P. C. van Zijl, *J. Biomol. NMR*, 1996, **7**, 77.
42. J. Zhou, B. Lal, D. A. Wilson, J. Laterra, and P. C. van Zijl, *Magn. Reson. Med.*, 2003, **50**, 1120.
43. J. Zhou, J. F. Payen, D. A. Wilson, R. J. Traystman, and P. C. van Zijl, *Nat. Med.*, 2003, **9**, 1085.
44. T. L. Hwang, P. C. van Zijl, and S. Mori, *J. Biomol. NMR*, 1998, **11**, 221.
45. G. Otting, E. Liepinsh, and K. Wuthrich, *Science*, 1991, **254**, 974.
46. K. L. Behar, D. L. Rothman, D. D. Spencer, and O. A. Petroff, *Magn. Reson. Med.*, 1994, **32**, 294.
47. R. A. Kauppinen, T. Niskanen, J. Hakumaki, and S. R. Williams, *NMR Biomed.*, 1993, **6**, 242.
48. G. Liu, M. Moake, Y. E. Har-el, C. M. Long, K. W. Chan, A. Cardona, M. Jamil, P. Walczak, A. A. Gilad, G. Sgouros, P. C. van Zijl, J. W. Bulte, and M. T. McMahon, *Magn. Reson. Med.*, 2012, **67**, 1106.
49. T. Shah, L. Lu, K. M. Dell, M. D. Pagel, M. A. Griswold, and C. A. Flask, *Magn. Reson. Med.*, 2011, **65**, 432.
50. H. Zhu, C. K. Jones, P. C. van Zijl, P. B. Barker, and J. Zhou, *Magn. Reson. Med.*, 2010, **64**, 638.
51. R. G. Bryant, *Annu. Rev. Biophys. Biomol. Struct.*, 1996, **25**, 29.
52. D. P. Hinton and R. G. Bryant, *Magn. Reson. Med.*, 1996, **35**, 497.
53. K. L. Desmond and G. J. Stanisz, *Magn. Reson. Med.*, 2012, **67**, 979.
54. J. Hua, C. K. Jones, J. Blakeley, S. A. Smith, P. C. van Zijl, and J. Zhou, *Magn. Reson. Med.*, 2007, **58**, 786.
55. J. Pekar, P. Jezzard, D. A. Roberts, J. S.Leigh Jr, J. A. Frank, and A. C. McLaughlin, *Magn. Reson. Med.*, 1996, **35**, 70.
56. S. Swanson and Y. Pang, *Proceedings of the 11th Annual Meeting ISMRM*, 2003.
57. A. X. Li, R. H. Hudson, J. W. Barrett, C. K. Jones, S. H. Pasternak, and R. Bartha, *Magn. Reson. Med.*, 2008, **60**, 1197.
58. P. Z. Sun, P. C. van Zijl, and J. Zhou, *J. Magn. Reson.*, 2005, **175**, 193.
59. P. Z. Sun, Y. Wang, Z. Dai, G. Xiao, and R. Wu, *Contrast Media Mol. Imaging*, 2014, **9**, 268.
60. D. E. Woessner, S. Zhang, M. E. Merritt, and A. D. Sherry, *Magn. Reson. Med.*, 2005, **53**, 790.
61. M. Zaiss, Z. Zu, J. Xu, P. Schuenke, D. F. Gochberg, J. C. Gore, M. E. Ladd, and P. Bachert, *NMR Biomed.*, 2015, **28**, 217.
62. J. Zhou, D. A. Wilson, P. Z. Sun, J. A. Klaus, and P. C. Van Zijl, *Magn. Reson. Med.*, 2004, **51**, 945.
63. R. S. Balaban and T. L. Ceckler, *Magn. Reson. Q.*, 1992, **8**, 116.
64. R. M. Henkelman, X. Huang, Q. S. Xiang, G. J. Stanisz, S. D. Swanson, and M. J. Bronskill, *Magn. Reson. Med.*, 1993, **29**, 759.
65. R. M. Henkelman, G. J. Stanisz, and S. J. Graham, *NMR Biomed.*, 2001, **14**, 57.
66. M. Woods, D. E. Woessner, and A. D. Sherry, *Chem. Soc. Rev.*, 2006, **35**, 500.
67. E. Liepinsh and G. Otting, *Magn. Reson. Med.*, 1996, **35**, 30.
68. W. Ling, R. R. Regatte, G. Navon, and A. Jerschow, *Proc. Natl. Acad. Sci. U. S. A.*, 2008, **105**, 2266.
69. J. Xu, N. N. Yadav, A. Bar-Shir, C. K. Jones, K. W. Chan, J. Zhang, P. Walczak, M. T. McMahon, and P. C. van Zijl, *Magn. Reson. Med.*, 2014, **71**, 1798.
70. T. Jin, J. Autio, T. Obata, and S. G. Kim, *Magn. Reson. Med.*, 2011, **65**, 1448.
71. C. K. Jones, D. Polders, J. Hua, H. Zhu, H. J. Hoogduin, J. Zhou, P. Luijten, and P. C. van Zijl, *Magn. Reson. Med.*, 2012, **67**, 1579.
72. C. K. Jones, A. Huang, J. Xu, R. A. Edden, M. Schar, J. Hua, N. Oskolkov, D. Zaca, J. Zhou, M. T. McMahon, J. J. Pillai, and P. C. van Zijl, *Neuroimage*, 2013, **77**, 114.
73. X. Xu, N. N. Yadav, H. Zeng, C. K. Jones, J. Zhou, P. C. van Zijl, and J. Xu, *Magn. Reson. Med.*, 2016, **75**, 88.
74. K. Snoussi, J. S. Gillen, A. Horska, N. A. Puts, S. Pradhan, R. A. Edden, and P. B. Barker, *Magn. Reson. Med.*, 2015, **74**, 607.
75. Z. Zu, K. Li, V. A. Janve, M. D. Does, and D. F. Gochberg, *Magn. Reson. Med.*, 2011, **66**, 1100.
76. J. C. McGowan, *Neurology*, 1999, **53**, S3.
77. G. B. Pike, *Magn. Reson. Med.*, 1996, **36**, 95.
78. N. P. Davies, I. R. Summers, and W. Vennart, *J. Magn. Reson. Imaging*, 2000, **11**, 539.
79. S. J. Graham and R. M. Henkelman, *Radiology*, 1999, **212**, 903.
80. B. S. Hu, S. M. Conolly, G. A. Wright, D. G. Nishimura, and A. Macovski, *Magn. Reson. Med.*, 1992, **26**, 231.
81. J. C.McGowan III, M. D. Schnall, and J. S. Leigh, *J. Magn. Reson. Imaging*, 1994, **4**, 79.
82. G. B. Pike, G. H. Glover, B. S. Hu, and D. R. Enzmann, *J. Magn. Reson. Imaging*, 1993, **3**, 531.
83. S. A. Smith, J. A. Farrell, C. K. Jones, D. S. Reich, P. A. Calabresi, and P. C. van Zijl, *Magn. Reson. Med.*, 2006, **56**, 866.
84. H. N. Yeung and A. M. Aisen, *Radiology*, 1992, **183**, 209.
85. D. F. Gochberg and J. C. Gore, *Magn. Reson. Med.*, 2003, **49**, 501.
86. D. F. Gochberg and J. C. Gore, *Magn. Reson. Med.*, 2007, **57**, 437.
87. P. Z. Sun, T. Benner, A. Kumar, and A. G. Sorensen, *Magn. Reson. Med.*, 2008, **60**, 834.
88. P. Z. Sun, J. Zhou, W. Sun, J. Huang, and P. C. van Zijl, *J. Cereb. Blood Flow Metab.*, 2007, **27**, 1129.
89. E. Vinogradov, H. He, A. Lubag, J. A. Balschi, A. D. Sherry, and R. E. Lenkinski, *Magn. Reson. Med.*, 2007, **58**, 650.
90. E. Vinogradov, S. Zhang, A. Lubag, J. A. Balschi, A. D. Sherry, and R. E. Lenkinski, *J. Magn. Reson.*, 2005, **176**, 54.
91. R. Scheidegger, E. Vinogradov, and D. C. Alsop, *Magn. Reson. Med.*, 2011, **66**, 1275.
92. G. Varma, G. Duhamel, C. de Bazelaire, and D. C. Alsop, *Magn. Reson. Med.*, 2015, **73**, 614.
93. J. Narvainen, P. L. Hubbard, R. A. Kauppinen, and G. A. Morris, *J. Magn. Reson.*, 2010, **207**, 242.
94. J. S. Lee, A. K. Khitrin, R. R. Regatte, and A. Jerschow, *J. Chem. Phys.*, 2011, **134**, 234504.
95. J. S. Lee, R. R. Regatte, and A. Jerschow, *J. Magn. Reson.*, 2012, **215**, 56.
96. X. Song, A. A. Gilad, S. Joel, G. Liu, A. Bar-Shir, Y. Liang, M. Gorelik, J. J. Pekar, P. C. van Zijl, J. W. Bulte, and M. T. McMahon, *Magn. Reson. Med.*, 2012, **68**, 1074.
97. X. Song, J. Xu, S. Xia, N. N. Yadav, B. Lal, J. Laterra, J. W. Bulte, P. C. van Zijl, and M. T. McMahon, *Magn. Reson. Med.*, 2015, **73**, 488.
98. M. T. McMahon, A. A. Gilad, J. Zhou, P. Z. Sun, J. W. Bulte, and P. C. van Zijl, *Magn. Reson. Med.*, 2006, **55**, 836.

99. E. Vinogradov, T. C. Soesbe, J. A. Balschi, A. D. Sherry, and R. E. Lenkinski, *J. Magn. Reson.*, 2012, **215**, 64.
100. J. I. Friedman, M. T. McMahon, J. T. Stivers, and P. C. Van Zijl, *J. Am. Chem. Soc.*, 2010, **132**, 1813.
101. Z. Zu, V. A. Janve, J. Xu, M. D. Does, J. C. Gore, and D. F. Gochberg, *Magn. Reson. Med.*, 2013, **69**, 637.
102. Z. Zu, J. Xu, H. Li, E. Y. Chekmenev, C. C. Quarles, M. D. Does, J. C. Gore, and D. F. Gochberg, *Magn. Reson. Med.*, 2014, **72**, 471.
103. N. N. Yadav, C. K. Jones, J. Hua, J. Xu, and P. C. van Zijl, *Magn. Reson. Med.*, 2013, **69**, 966.
104. C. Y. Lin, N. N. Yadav, J. I. Friedman, J. Ratnakar, A. D. Sherry, and P. C. van Zijl, *Magn. Reson. Med.*, 2012, **67**, 906.
105. C. Y. Lin, N. N. Yadav, J. Ratnakar, A. D. Sherry, and P. C. van Zijl, *Magn. Reson. Med.*, 2014, **71**, 286.
106. J. I. Friedman, D. Xia, R. R. Regatte, and A. Jerschow, *J. Magn. Reson.*, 2015, **256**, 43.
107. N. N. Yadav, C. K. Jones, J. Xu, A. Bar-Shir, A. A. Gilad, M. T. McMahon, and P. C. van Zijl, *Magn. Reson. Med.*, 2012, **68**, 1048.
108. J. Xu, K. W. Y. Chan, X. Xu, N. Yadav, G. Liu, and P. C. M. van Zijl, *Magn. Reson. Med.*, 2016. DOI: 10.1002/mrm.26165.
109. X. Xu, K. W. Chan, L. Knutsson, D. Artemov, J. Xu, G. Liu, Y. Kato, B. Lal, J. Laterra, M. T. McMahon, and P. C. van Zijl, *Magn. Reson. Med.*, 2015, **74**, 1556.
110. X. Xu, N. Yadav, L. Knutsson, J. Hua, R. Kalyani, E. Hall, J. Laterra, J. Blakeley, R. Strowd, M. Pomper, P. Barker, K. W. Chan, G. Liu, M. T. McMahon, R. D. Stevens, and P. C. van Zijl, *Tomography*, 2015, **1**, 105.
111. P. Z. Sun, J. Zhou, W. Sun, J. Huang, and P. C. van Zijl, *Magn. Reson. Med.*, 2005, **54**, 222.
112. J. Zhou, J. O. Blakeley, J. Hua, M. Kim, J. Laterra, M. G. Pomper, and P. C. van Zijl, *Magn. Reson. Med.*, 2008, **60**, 842.
113. P. Z. Sun, C. T. Farrar, and A. G. Sorensen, *Magn. Reson. Med.*, 2007, **58**, 1207.
114. M. Kim, J. Gillen, B. A. Landman, J. Zhou, and P. C. van Zijl, *Magn. Reson. Med.*, 2009, **61**, 1441.
115. C. O. Miller, J. Cao, E. Y. Chekmenev, B. M. Damon, A. D. Cherrington, and J. C. Gore, *Anal. Chem.*, 2015, **87**, 5824.
116. P. C. van Zijl, C. K. Jones, J. Ren, C. R. Malloy, and A. D. Sherry, *Proc. Natl. Acad. Sci. U. S. A.*, 2007, **104**, 4359.
117. K. W. Chan, M. T. McMahon, Y. Kato, G. Liu, J. W. Bulte, Z. M. Bhujwalla, D. Artemov, and P. C. van Zijl, *Magn. Reson. Med.*, 2012, **68**, 1764.
118. S. Walker-Samuel, R. Ramasawmy, F. Torrealdea, M. Rega, V. Rajkumar, S. P. Johnson, S. Richardson, M. Goncalves, H. G. Parkes, E. Arstad, D. L. Thomas, R. B. Pedley, M. F. Lythgoe, and X. Golay, *Nat. Med.*, 2013, **19**, 1067.
119. G. Liu, Y. Li, and M. D. Pagel, *Magn. Reson. Med.*, 2007, **58**, 1249.
120. M. Zaiss, B. Schmitt, and P. Bachert, *J. Magn. Reson.*, 2011, **211**, 149.
121. N. N. Yadav, K. W. Chan, C. K. Jones, M. T. McMahon, and P. C. van Zijl, *Magn. Reson. Med.*, 2013, **70**, 547.
122. T. Jin, P. Wang, X. Zong, and S. G. Kim, *Magn. Reson. Med.*, 2013, **69**, 760.
123. C. B. Lauzon, P. van Zijl, and J. T. Stivers, *J. Biomol. NMR*, 2011, **50**, 299.
124. G. Liu, K. W. Chan, X. Song, J. Zhang, A. A. Gilad, J. W. Bulte, P. C. van Zijl, and M. T. McMahon, *Magn. Reson. Med.*, 2013, **69**, 516.
125. K. L. Desmond, F. Moosvi, and G. J. Stanisz, *Magn. Reson. Med.*, 2014, **71**, 1841.
126. H. Y. Heo, Y. Zhang, S. Jiang, D. H. Lee, and J. Zhou, *Magn. Reson. Med.*, 2016, **75**, 1630.
127. R. Scheidegger, E. T. Wong, and D. C. Alsop, *Neuroimage*, 2014, **99**, 256.
128. J. Xu, M. Zaiss, Z. Zu, H. Li, J. Xie, D. F. Gochberg, P. Bachert, and J. C. Gore, *NMR Biomed.*, 2014, **27**, 406.
129. K. Yan, Z. Fu, C. Yang, K. Zhang, S. Jiang, D. H. Lee, H. Y. Heo, Y. Zhang, R. N. Cole, J. E. Van Eyk, and J. Zhou, *Mol. Imaging Biol.*, 2015, **17**, 479.
130. M. Zaiss, J. Windschuh, D. Paech, J. E. Meissner, S. Burth, B. Schmitt, P. Kickingereder, B. Wiestler, W. Wick, M. Bendszus, H. P. Schlemmer, M. E. Ladd, P. Bachert, and A. Radbruch, *Neuroimage*, 2015, **112**, 180.
131. M. Zaiss, J. Xu, S. Goerke, I. S. Khan, R. J. Singer, J. C. Gore, D. F. Gochberg, and P. Bachert, *NMR Biomed.*, 2014, **27**, 240.
132. W. T. Dixon, J. Ren, A. J. Lubag, J. Ratnakar, E. Vinogradov, I. Hancu, R. E. Lenkinski, and A. D. Sherry, *Magn. Reson. Med.*, 2010, **63**, 625.
133. A. Singh, K. Cai, M. Haris, H. Hariharan, and R. Reddy, *Magn. Reson. Med.*, 2013, **69**, 818.
134. J. Windschuh, M. Zaiss, J. E. Meissner, D. Paech, A. Radbruch, M. E. Ladd, and P. Bachert, *NMR Biomed.*, 2015, **28**, 529.
135. S. Aime, D. Delli Castelli, F. Fedeli, and E. Terreno, *J. Am. Chem. Soc.*, 2002, **124**, 9364.
136. S. Aime, D. Delli Castelli, and E. Terreno, *Angew. Chem. Int. Ed. Engl.*, 2005, **44**, 5513.
137. S. J. Dorazio, P. B. Tsitovich, K. E. Siters, J. A. Spernyak, and J. R. Morrow, *J. Am. Chem. Soc.*, 2011, **133**, 14154.
138. A. X. Li, F. Wojciechowski, M. Suchy, C. K. Jones, R. H. Hudson, R. S. Menon, and R. Bartha, *Magn. Reson. Med.*, 2008, **59**, 374.
139. A. O. Olatunde, J. M. Cox, M. D. Daddario, J. A. Spernyak, J. B. Benedict, and J. R. Morrow, *Inorg. Chem.*, 2014, **53**, 8311.
140. A. O. Olatunde, S. J. Dorazio, J. A. Spernyak, and J. R. Morrow, *J. Am. Chem. Soc.*, 2012, **134**, 18503.
141. E. Terreno, D. D. Castelli, and S. Aime, *Contrast Media Mol. Imaging*, 2010, **5**, 78.
142. E. Terreno, D. Delli Castelli, C. Cabella, W. Dastru, A. Sanino, J. Stancanello, L. Tei, and S. Aime, *Chem. Biodivers.*, 2008, **5**, 1901.
143. E. Terreno, D. Delli Castelli, E. Violante, H. M. Sanders, N. A. Sommerdijk, and S. Aime, *Chemistry*, 2009, **15**, 1440.
144. B. Yoo and M. D. Pagel, *J. Am. Chem. Soc.*, 2006, **128**, 14032.
145. B. Yoo and M. D. Pagel, *Front. Biosci.*, 2008, **13**, 1733.
146. B. Yoo, M. S. Raam, R. M. Rosenblum, and M. D. Pagel, *Contrast Media Mol. Imaging*, 2007, **2**, 189.
147. B. Yoo, V. R. Sheth, C. M. Howison, M. J. Douglas, C. T. Pineda, E. A. Maine, A. F. Baker, and M. D. Pagel, *Magn. Reson. Med.*, 2014, **71**, 1221.
148. S. Zhang, M. Merritt, D. E. Woessner, R. E. Lenkinski, and A. D. Sherry, *Acc. Chem. Res.*, 2003, **36**, 783.
149. K. Cai, M. Haris, A. Singh, F. Kogan, J. H. Greenberg, H. Hariharan, J. A. Detre, and R. Reddy, *Nat. Med.*, 2012, **18**, 302.
150. A. A. Gilad, M. T. McMahon, P. Walczak, P. T. Winnard Jr, V. Raman, H. W. van Laarhoven, C. M. Skoglund, J. W. Bulte, and P. C. van Zijl, *Nat. Biotechnol.*, 2007, **25**, 217.
151. M. Haris, K. Cai, A. Singh, H. Hariharan, and R. Reddy, *Neuroimage*, 2011, **54**, 2079.
152. M. Haris, A. Singh, K. Cai, F. Kogan, J. McGarvey, C. Debrosse, G. A. Zsido, W. R. Witschey, K. Koomalsingh, J. J. Pilla, J. A. Chirinos, V. A. Ferrari, J. H. Gorman, H. Hariharan, R. C. Gorman, and R. Reddy, *Nat. Med.*, 2014, **20**, 209.
153. C. K. Jones, M. J. Schlosser, P. C. van Zijl, M. G. Pomper, X. Golay, and J. Zhou, *Magn. Reson. Med.*, 2006, **56**, 585.
154. F. Kogan, M. Haris, A. Singh, K. Cai, C. Debrosse, R. P. Nanga, H. Hariharan, and R. Reddy, *Magn. Reson. Med.*, 2014, **71**, 164.
155. M. T. McMahon and K. W. Chan, *Adv. Cancer Res.*, 2014, **124**, 297.
156. M. T. McMahon, A. A. Gilad, M. A. DeLiso, S. M. Berman, J. W. Bulte, and P. C. van Zijl, *Magn. Reson. Med.*, 2008, **60**, 803.

157. P. Z. Sun, Y. Murata, J. Lu, X. Wang, E. H. Lo, and A. G. Sorensen, *Magn. Reson. Med.*, 2008, **59**, 1175.

158. P. Z. Sun and A. G. Sorensen, *Magn. Reson. Med.*, 2008, **60**, 390.

159. J. Zhou, E. Tryggestad, Z. Wen, B. Lal, T. Zhou, R. Grossman, S. Wang, K. Yan, D. X. Fu, E. Ford, B. Tyler, J. Blakeley, J. Laterra, and P. C. van Zijl, *Nat. Med.*, 2011, **17**, 130.

160. Z. Zu, V. A. Janve, K. Li, M. D. Does, J. C. Gore, and D. F. Gochberg, *Magn. Reson. Med.*, 2012, **68**, 711.

161. L. Schroder, T. J. Lowery, C. Hilty, D. E. Wemmer, and A. Pines, *Science*, 2006, **314**, 446.

162. T. K. Stevens, K. K. Palaniappan, R. M. Ramirez, M. B. Francis, D. E. Wemmer, and A. Pines, *Magn. Reson. Med.*, 2013, **69**, 1245.

163. S. Aime, D. Delli Castelli, D. Lawson, and E. Terreno, *J. Am. Chem. Soc.*, 2007, **129**, 2430.

164. J. M. Zhao, Y. E. Har-el, M. T. McMahon, J. Zhou, A. D. Sherry, G. Sgouros, J. W. Bulte, and P. C. van Zijl, *J. Am. Chem. Soc.*, 2008, **130**, 5178.

165. A. Salhotra, B. Lal, J. Laterra, P. Z. Sun, P. C. van Zijl, and J. Zhou, *NMR Biomed.*, 2008, **21**, 489.

166. H. Y. Heo, C. K. Jones, J. Hua, N. Yadav, S. Agarwal, J. Zhou, P. C. van Zijl, and J. J. Pillai, *J. Magn. Reson. Imaging*, 2015. DOI: 10.1002/jmri.25108.

167. J. Zhou, H. Zhu, M. Lim, L. Blair, A. Quinones-Hinojosa, S. A. Messina, C. G. Eberhart, M. G. Pomper, J. Laterra, P. B. Barker, P. C. van Zijl, and J. O. Blakeley, *J. Magn. Reson. Imaging*, 2013, **38**, 1119.

168. K. Sagiyama, T. Mashimo, O. Togao, V. Vemireddy, K. J. Hatanpaa, E. A. Maher, B. E. Mickey, E. Pan, A. D. Sherry, R. M. Bachoo, and M. Takahashi, *Proc. Natl. Acad. Sci. U. S. A.*, 2014, **111**, 4542.

169. M. Wang, X. Hong, C. F. Chang, Q. Li, B. Ma, H. Zhang, S. Xiang, H. Y. Heo, Y. Zhang, D. H. Lee, S. Jiang, R. Leigh, R. C. Koehler, P. C. van Zijl, J. Wang, and J. Zhou, *Magn. Reson. Med.*, 2015. DOI: 10.1002/mrm.25690.

170. J. E. Park, H. S. Kim, K. J. Park, C. G. Choi, and S. J. Kim, *Radiology*, 2015, **277**, 151.

171. J. E. Park, H. S. Kim, K. J. Park, S. J. Kim, J. H. Kim, and S. A. Smith, *Radiology*, 2015, **278**, 514.

172. O. Togao, T. Yoshiura, J. Keupp, A. Hiwatashi, K. Yamashita, K. Kikuchi, Y. Suzuki, S. O. Suzuki, T. Iwaki, N. Hata, M. Mizoguchi, K. Yoshimoto, K. Sagiyama, M. Takahashi, and H. Honda, *Neuro Oncol.*, 2014, **16**, 441.

173. Z. Wen, S. Hu, F. Huang, X. Wang, L. Guo, X. Quan, S. Wang, and J. Zhou, *Neuroimage*, 2010, **51**, 616.

174. D. W. Klomp, A. N. Dula, L. R. Arlinghaus, M. Italiaander, R. D. Dortch, Z. Zu, J. M. Williams, D. F. Gochberg, P. R. Luijten, J. C. Gore, T. E. Yankeelov, and S. A. Smith, *NMR Biomed.*, 2013, **26**, 1271.

175. G. Jia, R. Abaza, J. D. Williams, D. L. Zynger, J. Zhou, Z. K. Shah, M. Patel, S. Sammet, L. Wei, R. R. Bahnson, and M. V. Knopp, *J. Magn. Reson. Imaging*, 2011, **33**, 647.

176. J. Yuan, S. Chen, A. D. King, J. Zhou, K. S. Bhatia, Q. Zhang, D. K. Yeung, J. Wei, G. S. Mok, and Y. X. Wang, *NMR Biomed.*, 2014, **27**, 1239.

177. G. W. Harston, Y. K. Tee, N. Blockley, T. W. Okell, S. Thandeswaran, G. Shaya, F. Sheerin, M. Cellerini, S. Payne, P. Jezzard, M. Chappell, and J. Kennedy, *Brain*, 2015, **138**, 36.

178. W. Ling, U. Eliav, G. Navon, and A. Jerschow, *J. Magn. Reson.*, 2008, **194**, 29.

179. B. Schmitt, S. Zbyn, D. Stelzeneder, V. Jellus, D. Paul, L. Lauer, P. Bachert, and S. Trattnig, *Radiology*, 2011, **260**, 257.

180. I. Krusche-Mandl, B. Schmitt, L. Zak, S. Apprich, S. Aldrian, V. Juras, K. M. Friedrich, S. Marlovits, M. Weber, and S. Trattnig, *Osteoarthritis Cartilage*, 2012, **20**, 357.

181. A. Singh, M. Haris, K. Cai, V. B. Kassey, F. Kogan, D. Reddy, H. Hariharan, and R. Reddy, *Magn. Reson. Med.*, 2012, **68**, 588.

182. G. Saar, B. Zhang, W. Ling, R. R. Regatte, G. Navon, and A. Jerschow, *NMR Biomed.*, 2012, **25**, 255.

183. S. Haneder, S. R. Apprich, B. Schmitt, H. J. Michaely, S. O. Schoenberg, K. M. Friedrich, and S. Trattnig, *Eur. Radiol.*, 2013, **23**, 861.

184. A. Muller-Lutz, C. Schleich, G. Pentang, B. Schmitt, R. S. Lanzman, F. Matuschke, H. J. Wittsack, and F. Miese, *J. Magn. Reson. Imaging*, 2015. DOI: 10.1002/jmri.24945.

185. A. Muller-Lutz, C. Schleich, B. Schmitt, G. Antoch, F. Matuschke, M. Quentin, H. J. Wittsack, and F. Miese, *Magn. Reson. Imaging*, 2016, **34**, 271.

186. C. Schleich, A. Muller-Lutz, M. Eichner, B. Schmitt, F. Matuschke, B. Bittersohl, C. Zilkens, H. J. Wittsack, G. Antoch, and F. Miese, *Spine (Phila Pa 1976)*, 2016, **41**, 146.

187. X. Zhao, Z. Wen, F. Huang, S. Lu, X. Wang, S. Hu, D. Zu, and J. Zhou, *Magn. Reson. Med.*, 2011, **66**, 1033.

188. K. Cai, A. Singh, D. R. Roalf, R. P. Nanga, M. Haris, H. Hariharan, R. Gur, and R. Reddy, *NMR Biomed.*, 2013, **26**, 1278.

189. M. Haris, K. Nath, K. Cai, A. Singh, R. Crescenzi, F. Kogan, G. Verma, S. Reddy, H. Hariharan, E. R. Melhem, and R. Reddy, *NMR Biomed.*, 2013, **26**, 386.

190. F. Kogan, A. Singh, C. Debrosse, M. Haris, K. Cai, R. P. Nanga, M. Elliott, H. Hariharan, and R. Reddy, *Neuroimage*, 2013, **77**, 262.

191. K. A. Davis, R. P. Nanga, S. Das, S. H. Chen, P. N. Hadar, J. R. Pollard, T. H. Lucas, R. T. Shinohara, B. Litt, H. Hariharan, M. A. Elliott, J. A. Detre, and R. Reddy, *Sci. Transl. Med.*, 2015, **7**, 309ra161.

192. M. Haris, R. P. Nanga, A. Singh, K. Cai, F. Kogan, H. Hariharan, and R. Reddy, *NMR Biomed.*, 2012, **25**, 1305.

193. F. Kogan, M. Haris, C. Debrosse, A. Singh, R. P. Nanga, K. Cai, H. Hariharan, and R. Reddy, *J. Magn. Reson. Imaging*, 2014, **40**, 596.

194. J. C. Gore, M. S. Brown, C. T. Mizumoto, and I. M. Armitage, *Magn. Reson. Med.*, 1986, **3**, 463.

195. N. N. Yadav, J. Xu, A. Bar-Shir, Q. Qin, K. W. Chan, K. Grgac, W. Li, M. T. McMahon, and P. C. van Zijl, *Magn. Reson. Med.*, 2014, **72**, 823.

196. S. Z. Chen, J. Yuan, M. Deng, J. Wei, J. Zhou, and Y. J. Wang, *Eur. Radiol.*, 2015. DOI: 10.1007/s00330-015-3972-0.

197. M. Deng, S. Z. Chen, J. Yuan, Q. Chan, J. Zhou, and Y. J. Wang, *Mol. Imaging Biol.*, 2016, **18**, 274.

198. C. H. Liu, A. Sastre, R. Conroy, B. Seto, and R. I. Pettigrew, *Mol. Imaging Biol.*, 2014, **16**, 595.

199. S. Aime, L. Calabi, L. Biondi, M. De Miranda, S. Ghelli, L. Paleari, C. Rebaudengo, and E. Terreno, *Magn. Reson. Med.*, 2005, **53**, 830.

200. L. Q. Chen, C. M. Howison, J. J. Jeffery, I. F. Robey, P. H. Kuo, and M. D. Pagel, *Magn. Reson. Med.*, 2014, **72**, 1408.

201. D. L. Longo, A. Busato, S. Lanzardo, F. Antico, and S. Aime, *Magn. Reson. Med.*, 2012. DOI: 10.1002/mrm.24513. [Epub ahead of print].

202. B. F. Moon, K. M. Jones, L. Q. Chen, P. Liu, E. A. Randtke, C. M. Howison, and M. D. Pagel, *Contrast Media Mol. Imaging*, 2015, **10**, 446.

203. A. Muller-Lutz, N. Khalil, B. Schmitt, V. Jellus, G. Pentang, G. Oeltzschner, G. Antoch, R. S. Lanzman, and H. J. Wittsack, *MAGMA*, 2014. DOI: 10.1007/s10334.

204. P. Z. Sun, D. L. Longo, W. Hu, G. Xiao, and R. Wu, *Phys. Med. Biol.*, 2014, **59**, 4493.

205. E. L. Lozner, A. W. Winkler, F. H. Taylor, and J. P. Peters, *J. Clin. Invest.*, 1941, **20**, 507.

206. F. A. Nasrallah, G. Pages, P. W. Kuchel, X. Golay, and K. H. Chuang, *J. Cereb. Blood Flow Metab.*, 2013, **33**, 1270.

207. M. Rivlin, I. Tsarfaty, and G. Navon, *Magn. Reson. Med.*, 2014, **72**, 1375.